A bin integral method for solving the kinetic collection equation

Lian-Ping Wang [a,*], Yan Xue [a], Wojciech W. Grabowski [b]

[a] *Department of Mechanical Engineering, University of Delaware, Newark, Delaware 19716, USA*
[b] *Mesoscale and Microscale Meteorology Division, National Center for Atmospheric Research, PO Box 3000, Boulder, CO 80307-3000, USA*

Abstract

A new numerical method for solving the kinetic collection equation (KCE) is proposed, and its accuracy and convergence are investigated. The method, herein referred to as the bin integral method with Gauss quadrature (BIMGQ), makes use of two binwise moments, namely, the number and mass concentration in each bin. These two degrees of freedom define an extended linear representation of the number density distribution for each bin following Enukashvily (1980). Unlike previous moment-based methods in which the gain and loss integrals are evaluated for a target bin, the concept of source–bin pair interactions is used to transfer bin moments from source bins to target bins. Collection kernels are treated by bilinear interpolations. All binwise interaction integrals are then handled exactly by Gauss quadrature of various orders. In essence the method combines favorable features in previous spectral moment-based and bin-based pair-interaction (or flux) methods to greatly enhance the logic, consistency, and simplicity in the numerical method and its implementation. Quantitative measures are developed to rigorously examine the accuracy and convergence properties of BIMGQ for both the Golovin kernel and hydrodynamic kernels. It is shown that BIMGQ has a superior accuracy for the Golovin kernel and a monotonic convergence behavior for hydrodynamic kernels. Direct comparisons are also made with the method of Berry and Reinhardt (1974), the linear flux method of Bott (1998), and the linear discrete method of Simmel et al. (2002).
© 2007 Elsevier Inc. All rights reserved.

1. Introduction

The kinetic collection equation (KCE) has long been used to mathematically model the time evolution of size distribution of droplets due to their collision-coalescence events [1]. In the absence of other processes

---

(e.g., condensational growth, breakup, etc.), KCE may be written in the form of a nonlinear integral-differential equation as

$$\frac{\partial n(x,t)}{\partial t} = \int_{x_1}^{x/2} n(x-y,t)K(x-y,y)n(y,t)\,\mathrm{d}y - \int_{x_1}^{\infty} n(x,t)K(x,y)n(y,t)\,\mathrm{d}y, \tag{1}$$

where $n(x,t)$ denotes the number concentration distribution, namely, $n(x,t)\,\mathrm{d}x$ denotes the number of particles per unit volume at time t with mass ranging from x to $x+\mathrm{d}x$; x_1 is the mass of the smallest particle in the system; and $K(x,y)$ is the collection kernel for interactions between particles of masses x and y. The first term on the right-hand side of Eq. (1) is referred to as the gain integral representing the production of mass-x particles due to all possible binary collision-coalescence events of smaller particles, and the second term is the loss integral resulting from collision-coalescence events involving mass-x particles as source particle. Typical applications of KCE include rain formation in warm clouds, production of titanium-dioxide pigments, fine spray combustion, polymerization, and formation of industrial emissions [2,3]. KCE is also known as the population balance equation, the Smoluchowski equation, or stochastic coalescence equation in various contexts in the literature.

For the purpose of later discussions of the numerical results, we introduce the integral moments of $n(x,t)$ of order k as

$$M_k(t) = \int_{x_1}^{\infty} x^k n(x,t)\,\mathrm{d}x, \quad k = 0, 1, 2, 3, \ldots \tag{2}$$

In the case of cloud droplets, the first three moments, $M_0(t)$, $M_1(t)$, and $M_2(t)$, have specific physical significance as they represent the total number concentration, liquid water content, and radar reflectivity [4]. The governing equations for the first three moments can be derived from Eq. (1), by noting the symmetry property of the collection kernel [i.e., $K(y,x) = K(x,y)$], yielding [4,5]

$$\frac{\mathrm{d}M_0(t)}{\mathrm{d}t} = -\frac{1}{2}\int_{x_1}^{\infty}\mathrm{d}x\int_{x_1}^{\infty}\mathrm{d}y\, n(x,t)K(x,y)n(y,t), \tag{3}$$

$$\frac{\mathrm{d}M_1(t)}{\mathrm{d}t} = 0, \tag{4}$$

$$\frac{\mathrm{d}M_2(t)}{\mathrm{d}t} = \int_{x_1}^{\infty}\mathrm{d}x\int_{x_1}^{\infty}\mathrm{d}y\, xy n(x,t)K(x,y)n(y,t). \tag{5}$$

It follows that the number density $M_0(t)$ is monotonically decreasing, the mass density $M_1(t)$ is a constant (e.g., mass conservation), and the radar reflectivity $M_2(t)$ and all higher order moments are monotonically increasing. These properties of KCE are well known and are physically associated with the monotonic shifting of the size distribution to larger sizes over time.

Other than the above general properties, the exact evolution of the size distribution depends on the nature of the two-dimensional collision kernel $K(x,y)$ and the initial size distribution. Analytical solutions to KCE have only been found for several very simple forms of $K(x,y)$ [6,5,7–11], a detailed review of which can be found in [12]. For realistic forms of the collection kernel for cloud droplets, such as the Long kernel [13] or the Hall kernel [14] often used for modeling gravitational coalescence in warm precipitating clouds, the time evolution of droplet size spectrum can only be obtained through the numerical solution of KCE.

It is well known that numerical solutions of KCE are subject to numerical diffusion and dispersion errors or a possible violation of overall mass conservation as expressed by Eq. (4) [15,16]. The numerical diffusion errors stem from inadequate representations of the local slope and curvature in the size distribution, while the numerical dispersion errors are caused by inaccurate relocations of mass classes after collision-coalescence events. If the gain and loss integrals are evaluated separately in a numerical method (e.g., the method of Berry and Reinhard [4]), the total mass of the system may not be conserved.

Over the years, three classes of numerical methods for solving KCE have emerged and they are summarized as follows. The first class is denoted here as *point-based methods*. Examples include the high-order Lagrangian interpolation method of Berry and Reinhardt [4], the collocation method of Gelbard and Seinfeld [17], and the cubic spline interpolation method of Eyre et al. [18]. In these methods, the distribution function $n(x,t)$ or some

transformed form of $n(x,t)$ is defined on a set of discrete points. Efforts are made to represent as accurately as possible the continuous distribution function in terms of the values at the discrete points, in order to accurately evaluate the gain and loss integrals. Since the gain and loss integrals are treated separately, the main drawback of these methods is the lack of precise mass conservation, and this problem may be quite severe for realistic collection kernels when a small number of discrete points are used [13,17,18]. Furthermore, higher-order interpolation schemes such as the ones used in Berry and Reinhardt [4] could lead to numerical instability in the tail region of the size spectrum (e.g. [19]).

The second class refers to *spectral moment methods* pioneered by Bleck [20] and Enukashvily [21], and further developed by Tzivion et al. [16,22,23]. In these methods, the moments of the distribution function within a discrete size bin or section $x_i \leqslant x < x_{i+1}$

$$m_k(t;i) \equiv \int_{x_i}^{x_{i+1}} x^k n(x,t)\, \mathrm{d}x, \quad k = 0, 1, 2, \ldots \tag{6}$$

are to be found numerically, starting with the exact governing equation derivable from Eq. (1)

$$\frac{\partial m_k(t;i)}{\partial t} = \int_{x_i}^{x_{i+1}} x^k\, \mathrm{d}x \int_{x_1}^{x/2} n(x-y,t) K(x-y,y) n(y,t)\, \mathrm{d}y - \int_{x_i}^{x_{i+1}} x^k n(x,t)\, \mathrm{d}x \int_{x_1}^{\infty} K(x,y) n(y,t)\, \mathrm{d}y, \tag{7}$$

where x_i and x_{i+1} are the masses defining the left and right boundaries of bin i, respectively. We note that the right-hand side of (7) now involves two-dimensional or *area* integrals over a pair of masses, x and y. The goal in these methods is to represent the bin-based gain and loss integrals in Eq. (7) in terms of the spectral moments $m_k(t;i)$ themselves. Various approximate representations are made to the collision kernel function and to the distribution function within each bin [16,20–23]. The key concept and the main mathematical difficulty in spectral moment methods are illustrated in Fig. 1. The loss integral, i.e. the second term on the right-hand side of Eq. (7), can be evaluated in a straightforward manner since the boundaries of all subdomains coincide with the bin boundaries, namely, the vertical rectangular integration region for the loss integral is composed of subdomains formed by complete x and y bins. However, the gain term or the first term on the right-hand side of Eq. (7) for the same *target* bin being considered is integrated over an tilted quadrilateral
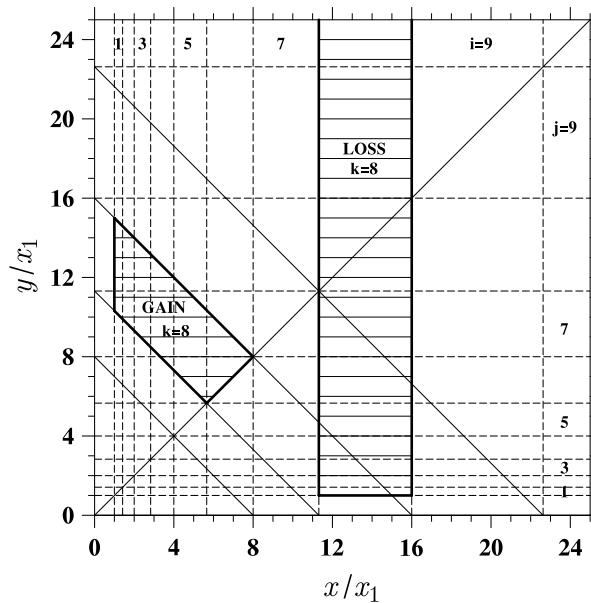

Fig. 1. An illustration of the domains of integration in spectral moment methods. Both mass axes are normalized by x_1 and a logarithmic bin distribution of mass ratio equal to $\sqrt{2}$ is assumed. The numbers on the right and top indicate the index number of a bin. Bin number 8 is the target bin considered. The lines with a slope of -1 indicate the boundaries of bins with mass equal to $(x+y)$. The tilted quadrilateral on the left indicates the domain of integration for the gain integral, and the vertical rectangular denotes the domain of integration for the loss integral.

domain (the region marked by GAIN in Fig. 1) whose boundaries do not coincide with bin boundaries (i.e., the integration limits problem), leading to often very lengthy expressions of the gain integral as in Enukashvily [21] and Tzivion et al. [16]. Furthermore, as a result of the integration limits problem, the gain integral requires computation of higher-order spectral moments than those explicitly considered (the so-called closure problem), and as such more closure approximations are necessary for the gain integral when compared to the loss integral. This fact implies that the mass conservation may not be guaranteed in actual implementation of spectral moment methods, although the error in the total mass is typically less than 1%, e.g., Tzivion et al. [22].

The early method by Bleck [20] considers only one spectral moment (the mass) in each bin, and the later ones by Enukashvily [21] and Tzivion et al. [16,22,23] employ two spectral moments (typically the number and mass in each bin). These studies recognize the need to represent accurately the distribution of $n(x, t)$ within a spectral bin, particularly in the tail region of the size distribution. For that purpose, polynomials of various orders or some combination of power law and polynomials have been attempted [16,20,23]. The detailed comparison study by Simmel et al. [24] seems to indicate that the spectral moment method is less accurate than other methods at a given bin resolution, although the convergence studies by Tzivion et al. [16,23] show a rapid convergence of their spectral moment method. Since Tzivion et al. [16,23] did not compare their converged solution directly with those of other methods, it is not clear if their converged solution is indeed the ground-truth solution.

While the above spectral moment methods derive themselves directly from the bin moment equations in their integral form, several related methods [25–28] have also been developed to preserve moments based on bin moment equations in their discrete form, in which the number or mass distribution in a bin is lumped together at a discrete location without explicit consideration of the number concentration distribution within a bin. These approaches can be formally linked to the integral form by using the mean value theorem of the calculus, see [27] for an overview. The first such approach was provided by Kovetz and Olund [25] who showed how to properly re-distribute a drop of a given volume created by collision-coalescence to two discrete drop size classes in such a way that both number and mass are conserved. Kumar and Ramkrishna in a sequence of papers [27–29] provided the most extensive and thorough development of two discrete moment methods called a fixed pivot technique and a moving pivot method. In their approaches, any two discrete moments can be chosen as the conserved properties and arbitrary mesh structure can be implemented.

The linear flux method of Bott [15] and the linear discrete method of Simmel et al. [24] fall into the third class which we shall term as *bin-based pair-interaction methods*. The basic idea of these methods is to break the contributions to the gain and loss integrals as a summation of a series of binary pair-interactions. The full *source* (rather than full target) bins, say i and j bins, are considered when considering the consequences of such binary pair-interactions, and the mass from the binary interaction is transferred into possibly two bins k and $k + 1$, as shown in Fig. 2. By design, the mass conservation is ensured through

$$\Delta m(i; i \leftrightarrow j) + \Delta m(j; i \leftrightarrow j) + \Delta m(k; i \leftrightarrow j) + \Delta m(k + 1; i \leftrightarrow j) = 0, \qquad (8)$$

where $\Delta m(l; i \leftrightarrow j)$ denotes the change of mass in bin l resulting from collision-coalescence events with i and j bins as source bins, namely, all binary collision-coalescence events of a droplet from bin i with a second droplet from bin j. Eq. (8) is the direct consequence of Eq. (4), when applied to the binary $i \leftrightarrow j$ interaction. Therefore, the gain and loss terms for the possibly four bins involved, i, j, k, and $k + 1$, are computed *simultaneously*. In numerical implementations, only three of the four terms in Eq. (8) need to be directly computed, and Eq. (8) may be used to evaluate the fourth term.

The domain of integration for the $i \leftrightarrow j$ interaction is indicated by the rectangular region marked by thick lines in Fig. 2. The right boundary of the k bin is represented by the line of $x + y = x_{k+1}$ and must necessarily cut through the rectangular region. The gain terms to bin k and $k + 1$ must be determined in terms of the distributions of $n(x, t)$ in the two source bins, bin i and bin j. However, in both the studies of Bott [15] and Simmel et al. [24], this important and logical connection was not made when they designed their scheme for redistributing the mass into k and $k + 1$ bins.

The purpose of this paper is to combine the favorable features in the spectral moment methods and in the bin-based pair-interaction methods. By doing so, we introduce rigor and logic to the bin-based pair-interaction methods. At the same time, the bin-based pair-interaction methods contain a simple and more logical treatment of the integration domains and greatly simplify the implementation details. The central question
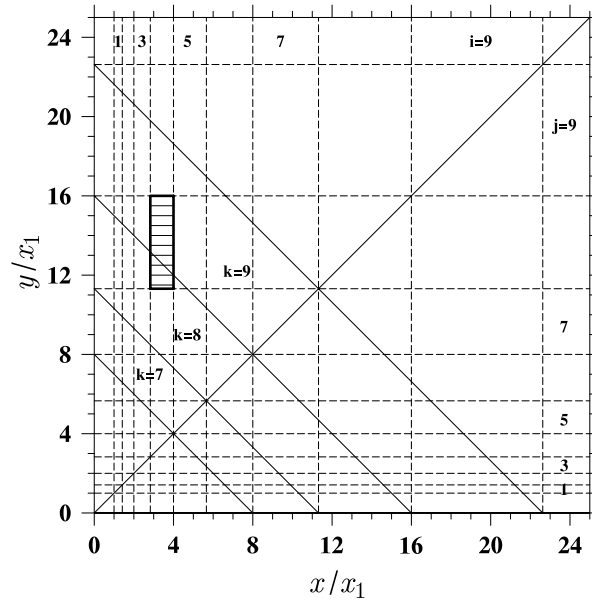
Fig. 2. An illustration of the domain of integration in bin-based pair-interaction methods due to the pair interaction between bin #4 and bin #8. The target bins are bin #8 and bin #9.

we will address is how the terms in Eq. (8) can be more logically and accurately computed, in order to design an accurate scheme with good convergence properties.

Our study is motivated by the need to obtain a numerically converged solution for KCE for an arbitrary collection kernel. The similar motivation has led Tzivion et al. [16] to compare numerical solutions using different bin resolutions. In this paper, we will simultaneously consider the converged solutions from our new method and three other methods including the method of Berry and Reinhardt (BRM) [4], the linear flux method (LFM) of Bott [15], and the linear discrete method (LDM) of Simmel et al. [24]. We will also develop quantitative measures of numerical errors in these approaches, based on a demonstrated ground-truth solution.

Obtaining the ground-truth solution free of numerical errors is particularly important in order to quantify the impact of the modified collection kernel due to air turbulence on the warm rain process [2,30]. This is because the collection kernel $K(x, y)$ for $x \neq y$ with a fine bin resolution can vary by 13 orders of magnitude when the radii of droplets are varied from 10 to 60 μm, and because the air turbulence tends to modify the collection kernel $K(x, y)$ selectively in the two-dimensional space (x, y) [31–33]. Such a strongly nonlinear collection kernel leads to an explosive growth, multiple peaks in $n(x, t)$, and exponential advancing fronts, all of which challenge the accurate numerical integration of KCE. An accurate method for KCE is also necessary when addressing the deviation of the spectral size distribution due to the true stochastic nature of the collision-coalescence process [34–36], when the numerical solution of KCE is compared to results based on Monte-Carlo simulations [37,38].

The details of our bin integral method with Gauss quadrature (BIMGQ) will be described in Section 2. Results and comparisons using the Golovin kernel will be presented in Section 3.1. In Section 3.2, numerical results using the Long kernel and the Hall kernel will be discussed. Numerical accuracy and convergence are discussed in Section 3.3. Conclusions and possible future developments will be outlined in Section 4.

2. The BIMGQ method

2.1. The concept and formulation

For computational efficiency, the mass (or radius) is discretized on a logarithmic scale, namely, the following geometric grid is used to define the bin boundary locations

$$x_i \equiv x_1 \rho^{i-1} \quad \text{for } i = 1, 2, 3, \ldots, N_{\text{bin}} + 1; \tag{9}$$

and the ith bin or section covers the mass range $x_i \leqslant x < x_{i+1}$. N_{bin} is the total number of bins assigned to cover an adequate size range. The mass ratio ρ is chosen to be

$$\frac{x_{i+1}}{x_i} \equiv \rho \equiv 2^{1/s}. \tag{10}$$

For convenience of handling self interactions, we shall assume that s is an integer, so that the self collision-coalescence interactions of particles in bin i will lead only to transfer of mass from bin i to bin $(i + s)$.

We first recognize that the gain and loss integrals in the spectral moment equation, Eq. (7), can be treated as summations of bin-based pair-interactions, as in Bott [15] and Simmel et al. [24]. All collision-coalescence events can be accounted for by taking the following summation:

$$\sum_{i=1}^{M} \sum_{j=i}^{M} i \leftrightarrow j, \tag{11}$$

where M ($M \leqslant N_{\text{bin}}$) denotes the current maximum bin number, at time t, for which there is a non-zero bin mass density (set by a small prescribed threshold). The value of M can increase with t as the size distribution is broadened. Note that $j \geqslant i$ in the above summation to avoid double-counting. Following Simmel et al. [24], we shall assume that the zeroth moment and the first moment in each bin are the two prognostic variables to be numerically solved:

$$\tilde{n}(t; i) \equiv m_0(t; i) = \int_{x_i}^{x_{i+1}} n(x, t; i) \, dx, \qquad \tilde{m}(t; i) \equiv m_1(t; i) = \int_{x_i}^{x_{i+1}} x n(x, t; i) \, dx, \tag{12}$$

where $n(x, t; i)$ represents an approximation to the local number density distribution in the ith bin. More specifically, for any time step, we assume that $\tilde{n}(t; i)$ and $\tilde{m}(t; i)$ are known for $1 \leqslant i \leqslant M$. The goal is to solve $\tilde{n}(t + dt; i)$ and $\tilde{m}(t + dt; i)$ for $1 \leqslant i \leqslant M + s$, using the evolution equation, Eq. (7). For any positive function $n(x, t; i)$, we have the following realizability condition:

$$x_i \leqslant \frac{\tilde{m}(t; i)}{\tilde{n}(t; i)} \leqslant x_{i+1}, \quad \text{or} \quad 1 \leqslant \frac{\tilde{m}(t; i)}{x_i \tilde{n}(t; i)} \leqslant \rho. \tag{13}$$

The above goal is essentially the same as that in spectral moment methods involving two spectral moments [16,21,22]. The difference is that, while in spectral moment methods the full gain and loss integrals are evaluated separately for a given target bin, here we compute the gain and loss integrals in pieces using the pair-interaction concept. A pair-interaction may be a self interaction or more generally a cross-interaction involving two distinct source bins. A self interaction $i \leftrightarrow i$ causes changes to only two distinct bins, namely, a reduction of spectral content in bin i and an augmentation of spectral content in bin $i + s$. In the case of a cross-interaction $i \leftrightarrow j$ ($j > i$), the target can cover two consecutive bins, bin k and bin $(k + 1)$, with the target referring to bins for which this $i \leftrightarrow j$ cross-interaction results in a gain of spectral contents. The boundary x_{k+1} between bin k and bin $(k + 1)$ cuts through the range of mass of droplets formed by collision-coalescence events due to the $i \leftrightarrow j$ cross interaction, namely,

$$x_i + x_j < x_{k+1} < x_{i+1} + x_{j+1}. \tag{14}$$

For the geometric grid, the target cannot cover more than two bins since $x_{i+1} + x_{j+1} = (x_i + x_j)\rho$. Therefore, an $i \leftrightarrow j$ cross-interaction could possibly affect the spectral contents of four distinct bins (i, j, k, and $k + 1$) if $k > j$.

If, however, $x_i + x_j < \rho x_j$ or equivalently $(j - i) \ln \rho + \ln(\rho - 1) > 0$, then $k = j$, leading to spectral changes of only three distinct bins: i, j, and $j + 1$. This situation occurs, for example, when $\rho = \sqrt{2}$ and $(j - i) \geqslant 3$, a situation illustrated in Fig. 2. In our numerical implementation, however, we do not treat the case of $k = j$ any differently from the case of $k > j$.

Next we recognize that, with two degrees of freedom in each bin, a nonuniform local distribution $n(x, t; i)$ in each bin can be specified. Following Enukashvily [21], Eq. (12) can be inverted to provide the following extended linear distribution in the ith bin,

$$n(x,t;i) = \begin{cases} n_{1,i}\frac{x_{2,i}-x}{x_{2,i}-x_{1,i}} + n_{2,i}\frac{x-x_{1,i}}{x_{2,i}-x_{1,i}} & \text{for } x_{1,i} \leqslant x \leqslant x_{2,i}, \\ 0 & \text{otherwise,} \end{cases} \tag{15}$$

where the four unknown parameters $n_{1,i}$, $n_{2,i}$, $x_{1,i}$, and $x_{2,i}$ can be uniquely determined in terms of $\tilde{n}(t;i)$ and $\tilde{m}(t;i)$. Here $x_{1,i}$ and $x_{2,i}$ can be viewed as the effective bin boundary locations as far as the gain and loss integrals are concerned. The realizability condition, Eq. (13), implies only three possible scenarios. Fig. 3 illustrates these three scenarios according to the relative location of the mass-weighted particle size: (a) $x_i = x_{1,i} < x_{2,i} = x_{i+1}$, (b) $x_i = x_{1,i} < x_{2,i} < x_{i+1}$, and (c) $x_i < x_{1,i} < x_{2,i} = x_{i+1}$. In scenario (a), the distribution extends over the full bin and this occurs when $(2+\rho)/3 \leqslant \tilde{m}(t;i)/[x_i\tilde{n}(t;i)] \leqslant (1+2\rho)/3$, while scenarios (b) and (c) correspond to the conditions $1 \leqslant \tilde{m}(t;i)/[x_i\tilde{n}(t;i)] < (2+\rho)/3$ and $(1+2\rho)/3 < \tilde{m}(t;i)/[x_i\tilde{n}(t;i)] \leqslant \rho$, respectively. In scenarios (b) and (c), only a portion of the bin is used to specify the distribution, with the rest filled with zero value.

In terms of the linear distribution, $\tilde{n}(t;i)$ and $\tilde{m}(t;i)$ can be written as

$$\tilde{n}(t;i) = (x_{2,i} - x_{1,i})\frac{n_{1,i} + n_{2,i}}{2}, \tag{16}$$

$$\tilde{m}(t;i) = (x_{2,i} - x_{1,i})\left[n_{1,i}\frac{2x_{1,i} + x_{2,i}}{6} + n_{2,i}\frac{x_{1,i} + 2x_{2,i}}{6}\right]. \tag{17}$$

The inversion formula under different scenarios can now be summarized. For scenario (a), we have

$$\begin{aligned} x_{1,i} &= x_i, \qquad x_{2,i} = x_{i+1}, \\ n_{1,i} &= 2[\tilde{n}(t;i)(x_i + 2x_{i+1}) - 3\tilde{m}(t;i)]/(\Delta x)^2, \\ n_{2,i} &= 2[-\tilde{n}(t;i)(2x_i + x_{i+1}) + 3\tilde{m}(t;i)]/(\Delta x)^2, \end{aligned} \tag{18}$$

where $\Delta x \equiv x_{i+1} - x_i$. The inversion formula under scenario (b) are

$$\begin{aligned} x_{1,i} &= x_i, \quad x_{2,i} = x_i + 3[\tilde{m}(t;i)/\tilde{n}(t;i) - x_i], \\ n_{1,i} &= \frac{2\tilde{n}(t;i)}{3[\tilde{m}(t;i)/\tilde{n}(t;i) - x_i]}, \quad n_{2,i} = 0. \end{aligned} \tag{19}$$

Finally, the expressions for scenario (c) are

$$\begin{aligned} x_{1,i} &= x_{i+1} - 3[x_{i+1} - \tilde{m}(t;i)/\tilde{n}(t;i)], \quad x_{2,i} = x_{i+1}, \\ n_{1,i} &= 0, \quad n_{2,i} = \frac{2\tilde{n}(t;i)}{3[x_{i+1} - \tilde{m}(t;i)/\tilde{n}(t;i)]}. \end{aligned} \tag{20}$$

The above demonstrates the equivalence of the locally extended linear distribution, Eq. (15), and its specification by the two moments $\tilde{n}(t;i)$ and $\tilde{m}(t;i)$. Since the bin-level distribution is explicitly prescribed, all higher order moments can be expressed using the distribution parameters. In general, the kth-order moment in the ith bin can be computed as

$$m_k(t;i) \equiv \int_{x_i}^{x_{i+1}} x^k n(x,t;i)\, dx = \frac{x_{2,i} - x_{1,i}}{(k+1)(k+2)}\left[n_{1,i}\sum_{m=0}^{k}(k+1-m)x_{1,i}^{k-m}x_{2,i}^{m} + n_{2,i}\sum_{m=0}^{k}(k+1-m)x_{2,i}^{k-m}x_{1,i}^{m}\right]. \tag{21}$$
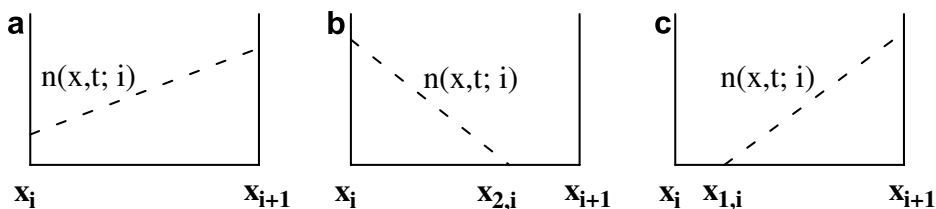

Fig. 3. The three possible scenarios of the extended linear function.

The basic strategy in BIMGQ is to use the above extended linear distribution to calculate the right-hand side of Eq. (7) so that the two bin moments, $\tilde{n}(t;i)$ and $\tilde{m}(t;i)$, can be advanced in time. The right-hand side of Eq. (7) cannot be explicitly expressed in terms of m_k of the same order. In fact, the nonlinearity of the integrands and the complex nature of the collection kernel imply a closure problem of such moment-based formulation (e.g. [21]). To fully resolve the closure problem, we treat the collection kernel by the following bilinear interpolation

$$K(x,y) = K(x_i,x_j)\frac{(x-x_{i+1})(y-y_{j+1})}{(x_i-x_{i+1})(x_j-x_{j+1})} + K(x_{i+1},x_j)\frac{(x-x_i)(y-y_{j+1})}{(x_{i+1}-x_i)(x_j-x_{j+1})}$$
$$+ K(x_i,x_{j+1})\frac{(x-x_{i+1})(y-y_j)}{(x_i-x_{i+1})(x_{j+1}-x_j)} + K(x_{i+1},x_{j+1})\frac{(x-x_i)(y-y_j)}{(x_{i+1}-x_i)(x_{j+1}-x_j)}, \tag{22}$$

assuming that $K(x_i,x_j)$ is known for all combinations of bin boundary locations (x_i,x_j). This bilinear representation together with the extended linear representation for $n(x,t;i)$ fully specifies the integrands on the right-hand side of Eq. (7). The algorithm for carrying out the integrals in terms of a summation of all binary pair interactions will be developed next.

2.2. Transfer due to pair interactions

While in Eq. (7), the gain and loss terms are referred to a specific target bin, we shall consider all relevant bins together and re-group the transfer of number and mass by collision-coalescence in terms of all possible combinations of binary source bins. For a cross interaction $i \leftrightarrow j$, the reductions in number and mass of the source bins can be written as

$$\Delta\tilde{n}(i; i \leftrightarrow j) = \Delta\tilde{n}(j; i \leftrightarrow j) = -dt \int_{x_{1,i}}^{x_{2,i}} dx \int_{x_{1,j}}^{x_{2,j}} dy \, n(x,t;i)K(x,y)n(y,t;j), \tag{23}$$

$$\Delta\tilde{m}(i; i \leftrightarrow j) = -dt \int_{x_{1,i}}^{x_{2,i}} dx \int_{x_{1,j}}^{x_{2,j}} dy \, xn(x,t;i)K(x,y)n(y,t;j), \tag{24}$$

$$\Delta\tilde{m}(j; i \leftrightarrow j) = -dt \int_{x_{1,i}}^{x_{2,i}} dx \int_{x_{1,j}}^{x_{2,j}} dy \, yn(x,t;i)K(x,y)n(y,t;j). \tag{25}$$

The newly generated droplets are transferred to bin k and bin $k+1$, the augmentations of number and mass concentration in bin k and bin $k+1$ can be rigorously expressed as

$$\Delta\tilde{n}(k; i \leftrightarrow j) = dt \underbrace{\int\int}_{\Omega_k} dx \, dy \, n(x,t;i)K(x,y)n(y,t;j,) \tag{26}$$

$$\Delta\tilde{n}(k+1; i \leftrightarrow j) = dt \underbrace{\int\int}_{\Omega_{k+1}} dx \, dy \, n(x,t;i)K(x,y)n(y,t;j), \tag{27}$$

$$\Delta\tilde{m}(k; i \leftrightarrow j) = dt \underbrace{\int\int}_{\Omega_k} dx \, dy(x+y)n(x,t;i)K(x,y)n(y,t;j), \tag{28}$$

$$\Delta\tilde{m}(k+1; i \leftrightarrow j) = dt \underbrace{\int\int}_{\Omega_{k+1}} dx \, dy(x+y)n(x,t;i)K(x,y)n(y,t;j), \tag{29}$$

where Ω_k and Ω_{k+1} are the subregions of integration with $x + y = x_{k+1}$ as the dividing line (Fig. 4). The above expressions follow exactly from the kinetic moment equations, Eq. (7). Of importance is that the gain integrals for the target bins are all written in terms of the masses x and y of the source bins. The net change in number concentration due to the $i \leftrightarrow j$ binary interaction is
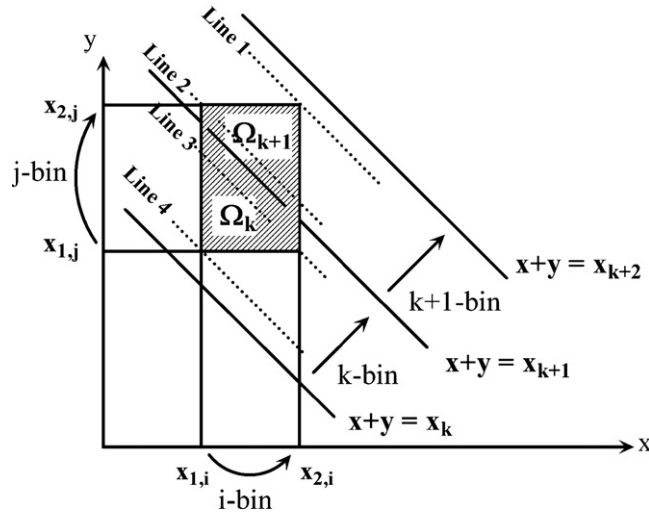
Fig. 4. Sketch showing domains of integration for the gain integral to k and $k + 1$ bins, respectively. The ranges of integration over x and y vary with the exact location of the line $x + y = x_{k+1}$ cutting through the shaded area, relative to the four dotted lines.

$$\Delta\tilde{n}(i; i \leftrightarrow j) + \Delta\tilde{n}(j; i \leftrightarrow j) + \Delta\tilde{n}(k; i \leftrightarrow j) + \Delta\tilde{n}(k + 1; i \leftrightarrow j)$$
$$= -\mathrm{d}t \int_{x_{1,i}}^{x_{2,i}} dx \int_{x_{1,j}}^{x_{2,j}} \mathrm{d}y\, n(x, t; i)K(x, y)n(y, t; j). \tag{30}$$

The net change in the system mass is zero, namely, Eq. (8) is satisfied. The conservation properties imply that it is sufficient to carry out only half of the integrations in Eq. (26)–(29), either the two over Ω_k or the two over Ω_{k+1}. When the line $x + y = x_{k+1}$ is located between the line +1 and line +2 in Fig. 4, it is more convenient to integrate over Ω_{k+1} to obtain the gain terms for bin $k + 1$ directly. On the other hand, if the line $x + y = x_{k+1}$ is located between the line 3 and line 4 in Fig. 4, only the gain terms over Ω_k are explicitly calculated. When the line $x + y = x_{k+1}$ is located between the line +2 and line +3, there is no preference as to which subregion should be performed directly.

For the $i \leftrightarrow i$ self-collision, the number and mass will be transferred from bin i to bin $i + s$, as follows:

$$\Delta\tilde{n}(i; i \leftrightarrow i) = -\mathrm{d}t \int_{x_{1,i}}^{x_{2,i}} \mathrm{d}x \int_{x_{1,i}}^{x_{2,i}} \mathrm{d}y\, n(x, t; i)K(x, y)n(y, t; i), \tag{31}$$

$$\Delta\tilde{m}(i; i \leftrightarrow i) = -\mathrm{d}t \int_{x_{1,i}}^{x_{2,i}} \mathrm{d}x \int_{x_{1,i}}^{x_{2,i}} \mathrm{d}y\, xn(x, t; i)K(x, y)n(y, t; i), \tag{32}$$

$$\Delta\tilde{n}(i + s; i \leftrightarrow i) = \frac{1}{2}\, \mathrm{d}t \int_{x_{1,i}}^{x_{2,i}} \mathrm{d}x \int_{x_{1,i}}^{x_{2,i}} \mathrm{d}y\, n(x, t; i)K(x, y)n(y, t; i), \tag{33}$$

$$\Delta\tilde{m}(i + s; i \leftrightarrow i) = -\Delta\tilde{m}(i; i \leftrightarrow i). \tag{34}$$

Therefore, there is no net change in the system mass, but the net change of the number due to the $i \leftrightarrow i$ self interaction is given as

$$\Delta\tilde{n}(i; i \leftrightarrow i) + \Delta\tilde{n}(i + s; i \leftrightarrow i) = -\frac{1}{2}\, \mathrm{d}t \int_{x_{1,i}}^{x_{2,i}} \mathrm{d}x \int_{x_{1,i}}^{x_{2,i}} \mathrm{d}y\, n(x, t; i)K(x, y)n(y, t; i). \tag{35}$$

The gain and loss integrals on the right-hand side of Eq. (7) can be evaluated by summing up all self and cross binary interactions according to Eq. (11).

2.3. Gauss quadrature

The remaining task is to perform the two-dimensional integrations for Eqs. (23)–(29) and Eqs. (31)–(34). Given the linear representations of $n(x, t; i)$ and $K(x, y)$, the integrands are all polynomials of two independent variables x and y. The orders of the polynomials are higher for the gain integrals due to the inclined boundary at $x + y = x_{k+1}$. In principle, these integrals can be performed analytically but it is tedious due to the number of terms involved. The Gauss quadrature formula is ideal for our purpose. In one dimension, the Gauss quadrature [39] is written as

$$\int_a^b f(x)\, dx = \frac{(b-a)}{2} \sum_{\alpha=1}^m A_\alpha^{(m)} f\left(\frac{b-a}{2} z_\alpha^{(m)} + \frac{a+b}{2}\right).$$

(36)

where m is the total number of Gauss quadrature points used. Here $z_\alpha^{(m)}$ ($\alpha = 1, 2, \ldots, m$) are Gauss quadrature abscissae defined in the domain $(-1, 1)$, and $A_\alpha^{(m)}$ are the weights. The values of $z_\alpha^{(m)}$ and $A_\alpha^{(m)}$ are available from standard text [39], and are listed in Table 1 in a form that would allow double-precision implementation. The Gauss quadrature formula is exact if $f(x)$ is a polynomial function of order $(2m - 1)$ or less.

The formula can be extended to two dimensions. For example, when the line $x + y = x_{k+1}$ is located between line 1 and line 2 in Fig. 4, the gain integral given by Eq. (29) can be computed exactly as

$$\Delta \tilde{m}(k+1; i \leftrightarrow j) = dt \int_{x_{k+1}-x_{2,j}}^{x_{2,i}} n(x, t; i)\, dx \int_{x_{k+1}-x}^{x_{2,j}} n(y, t; j) K(x, y)(x + y)\, dy$$

$$= dt \frac{x_{2,i} + x_{2,j} - x_{k+1}}{2} \sum_{\alpha=1}^4 A_\alpha^{(4)} n(x_\alpha^{(4)}) \frac{x_\alpha^{(4)} + x_{2,j} - x_{k+1}}{2} \sum_{\beta=1}^2 A_\beta^{(2)} n(y_{\alpha\beta}^{(2)}) K(x_\alpha^{(4)}, y_{\alpha\beta}^{(2)})(x_\alpha^{(4)} + y_{\alpha\beta}^{(2)}),$$

(37)

where

$$x_\alpha^{(4)} \equiv \frac{x_{2,i} - x_{k+1} + x_{2,j}}{2} z_\alpha^{(4)} + \frac{x_{2,i} + x_{k+1} - x_{2,j}}{2},$$

(38)

$$y_{\alpha\beta}^{(2)} \equiv \frac{x_{2,j} - x_{k+1} + x_\alpha^{(4)}}{2} z_\beta^{(2)} + \frac{x_{2,j} + x_{k+1} - x_\alpha^{(4)}}{2}.$$

(39)

In the above example, the integrand for the inner integral is a polynomial of order 3 in y, while the integrand for the outer integral is a polynomial of order 6 in x. The polynomial order for x takes into consideration that $y_{\alpha\beta}^{(2)}$ depends linearly on x due to the inclined boundary $x + y = x_{k+1}$. These lead to the choice for the number of Gauss quadrature points for the inner integral over y to 2 and for the outer integral over x to 4. Table 2 summarizes the orders of polynomials and the corresponding numbers of abscissae needed for different terms shown in Section 2.2, assuming that the integration over y is performed first.

Table 1
Exact expressions of Gauss quadrature abscissae and weights

Order (m)	Abscissae ($z_\alpha^{(m)}$)	Weights ($A_\alpha^{(m)}$)	Polynomials order ($2m - 1$)
1	0	2	1
2	$\pm\sqrt{\frac{1}{3}}$	1	3
3	0	$\frac{8}{9}$	5
	$\pm\sqrt{\frac{3}{5}}$	$\frac{5}{9}$	
4	$\pm\sqrt{\frac{15-2\sqrt{30}}{35}}$	$\frac{3\sqrt{30}+5}{6\sqrt{30}}$	7
	$\pm\sqrt{\frac{15+2\sqrt{30}}{35}}$	$\frac{3\sqrt{30}-5}{6\sqrt{30}}$	

Table 2
Polynomial order and the minimum number of Gauss quadrature points needed for the exact integration of the approximated gain and loss integrals

	Polynomial order		m	
	x	y	x	y
$\Delta\tilde{n}(i, i \leftrightarrow j) = \Delta\tilde{n}(j, i \leftrightarrow j)$	2	2	2	2
$\Delta\tilde{m}(i, i \leftrightarrow j)$	3	2	2	2
$\Delta\tilde{m}(j, i \leftrightarrow j)$	2	3	2	2
$\Delta\tilde{n}(k, i \leftrightarrow j)$	5	2	3	2
$\Delta\tilde{n}(k+1, i \leftrightarrow j)$	5	2	3	2
$\Delta\tilde{m}(k, i \leftrightarrow j)$	6	3	4	2
$\Delta\tilde{m}(k+1, i \leftrightarrow j)$	6	3	4	2
$\Delta\tilde{n}(i, i \leftrightarrow i)$	2	2	2	2
$\Delta\tilde{m}(i, i \leftrightarrow i)$	3	2	2	2
$\Delta\tilde{n}(i+s, i \leftrightarrow i)$	2	2	2	2
$\Delta\tilde{m}(i+s, i \leftrightarrow i)$	3	3	2	2

2.4. Summary of the numerical procedure

In summary, two bin moments (number and mass) are used in each bin to construct a locally extended linear distribution $n(x, t; i)$. This linear distribution in turn allows a consistent evaluation of the gain and loss integrals in the kinetic moment equations. The algorithm consists of the following steps:

Step 1. Set up bin boundaries x_i based on x_1 and ρ (or s) and define the initial conditions for $\tilde{n}(t = 0; i)$ and $\tilde{m}(t = 0; i)$ with a given initial distribution $n(x, t = 0)$.
Step 2. Construct a locally extended linear distribution $n(x, t; i)$ in each bin by the two bin moments $\tilde{n}(t; i)$ and $\tilde{m}(t; i)$.
Step 3. Apply Gauss Quadrature formulae to evaluate the gain and loss integrals for each cross pair interaction and each self interaction.
Step 4. Sum up all interactions to form the net gain and loss to $\tilde{n}(t; i)$ and $\tilde{m}(t; i)$ for each bin.
Step 5. Advance the two bin moments to obtain $\tilde{n}(t + dt; i)$ and $\tilde{m}(t + dt; i)$ by the Euler method.
Step 6. Repeat Step 2 through Step 5 until a desired time is reached.

3. Results and discussions

In this section, numerical solutions from BIMGQ will be examined in detail and compared with those from three other methods, namely, the method of Berry and Reinhardt (BRM) [4], the linear flux method of Bott (LFM) [15], and the linear discrete method (LDM) of Simmel et al. [24]. The LFM code contains an improvement over what was reported in [15], namely, with a local exponential fit in the form of $g = c_1 \exp(c_2 \ln r)$ being used for computing the mass splitting over the target bins. The exponential fit was found to yield optimal results in Bott's approach [24]. We will also compare all solutions to either analytical or converged solution and develop quantitative error measures to study the rate of convergence of each method.

Numerical solutions are often presented in terms of the mass distribution function $g(\ln r, t) \equiv 3x^2 n(x, t)$ over a logarithmic radius scale, such that the total mass is equal to the area under the $g(\ln r, t)$ curve, namely,

$$M_1(t) = \int g(\ln r, t) \, d(\ln r), \tag{40}$$

where r is the radius of droplets and is related to the mass by $r \equiv [3x/(4\pi\rho_w)]^{1/3}$. The water density ρ_w is set to 10^3 kg/m^3.

The solution of KCE depends on the initial distribution and the nature of collection kernel. The following initial size distribution

$$n(x, t = 0) = \frac{N_0}{\bar{x}_0} \exp\left(-\frac{x}{\bar{x}_0}\right), \quad \text{or} \quad g(\ln r, t = 0) = 3L_0 \left(\frac{x}{\bar{x}_0}\right)^2 \exp\left(-\frac{x}{\bar{x}_0}\right) \tag{41}$$

is used, similar to previous studies [4,15,24]. The above distribution is theoretically defined over $0 < x < \infty$, with the initial total number concentration N_0 and the initial mean mass $\bar{x}_0 \equiv L_0/N_0$. Here L_0 is the liquid water content (total liquid mass per unit volume). Following Simmel et al. [24], we set the initial mean radius $\bar{r}_0 \equiv (3\bar{x}_0/4\pi\rho_w)^{1/3}$ to 9.3 μm and L_0 to 1 g/m³. These correspond to $N_0 \approx 300$ cm^{-3} and $\bar{x}_0 \approx 3.37 \times 10^{-9}$ g.

Another parameter for the initial condition is the minimum droplet radius $r_1 \equiv [3x_1/(4\pi\rho_w)]^{1/3}$ considered. We chose $r_1 = 1.5625$ μm to ensure that the mass below x_1 in the above distribution is negligible. The truncated mass is $\int_0^{x_1} xn(x, t = 0)\,dx$ or $1.12 \times 10^{-5}L_0$, leaving the actual mass represented on the numerical grid to be 0.999989 g/m³. The time step size dt was set to 1 s.

3.1. Golovin kernel

We first consider the Golovin collection kernel with $K(x, y) = b(x + y)$ and $b = 1.5$ m³/(kg s). The Golovin kernel is often used to test different numerical methods for KCE since the analytical solution exists for this case [9] and it may be used as an approximation to the actual hydrodynamic kernel for large cloud droplets.

In order to clearly demonstrate the accuracy of BIMGQ, we shall first examine the salient properties of a collision-coalescence system governed by the Golovin kernel. In this case, Eqs. (3) and (4) can be shown to become

$$\frac{dM_0(t)}{dt} = -bM_0(t)M_1(t) = -bL_0M_0(t), \tag{42}$$

$$\frac{dM_1(t)}{dt} = 0. \tag{43}$$

Therefore, the system number density and mass density have the following analytical solutions:

$$M_0(t) = N_0 \exp(-bL_0t), \qquad M_1(t) = L_0. \tag{44}$$

It can be shown that, with our BIMGQ algorithm and the Euler scheme for time integration, these two global moments are updated, at each time step, as follows:

$$M_0(t + dt) - M_0(t) = -bM_0(t)L_0\,dt, \tag{45}$$
$$M_1(t + dt) - M_1(t) = 0. \tag{46}$$

Eq. (45) follows from the fact that the right-hand side of Eq. (3) can be written precisely as $-0.5b[\sum \tilde{m}(t; i) \sum \tilde{n}(t; i) + \sum \tilde{n}(t; i) \sum \tilde{m}(t; i)] = -bM_0(t)L_0$. These correspond *exactly* to the differential equations, Eqs. (46) and (47), if the same Euler scheme is used for time integration. Therefore, neglecting any numerical roundoff errors, the total number density from the BIMGQ algorithm evolves as

$$M_0(k\,dt) = (1 - bL_0\,dt)^k M_0(t = 0), \tag{47}$$

where k is the number of time steps. The mass conservation $M_1(k\,dt) = L_0$ is ensured by design, as in other bin-based pair-interaction (or flux) methods [15,24]. We initialize $\tilde{n}(t = 0; i)$ and $\tilde{m}(t = 0; i)$ using the definitions given by Eq. (12) with $n(x, t = 0)$ from Eq. (41).

The important observation here is that, for the Golovin kernel, our method treats both the zeroth-order and first-order moments exactly except the time integration error, *regardless* of the bin resolution (the parameter s) used. This is a consequence of the fact that Golovin kernel is itself a polynomial and is treated exactly in BIMGQ.

Fig. 5 compares the predicted total number, on a linear-log plot, with the analytical solution and the numerical solution of Simmel et al. [24]. With d$t = 1$ s, $bL_0dt = 0.0015$, the numerical solution given by Eq. (47) differs from the exact solution given by Eq. (44) by a factor $0.99925^{0.0015t}$ which is very close to one for all the times considered in Fig. 5, namely, dt is small enough and the time integration error for $M_0(k\,dt)$ is negligible. This is why the predicted total number by BIMGQ overlaps precisely with the analytical solution for the two bin resolutions ($s = 1$ and $s = 2$). The above analysis and the numerical results show that, for the case of Golovin kernel, not only does our method conserve mass exactly, it also predicts the total number exactly due to the consistency of the formulation with the moment equation. This excellent feature is not retained in the methods of Bott [15] and Simmel et al. [24], due to the fact that their methods for redistributing
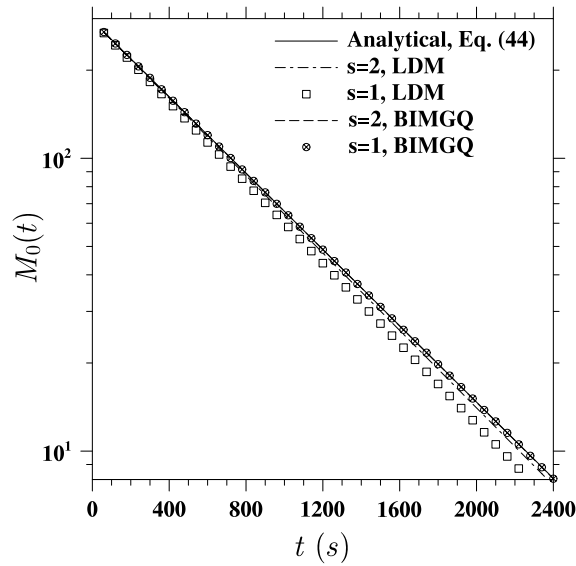
Fig. 5. The total number as a function of time for a collision-coalescence system driven by the Golovin kernel. Note that BIMGQ overlaps precisely with the analytical solution for both bin resolutions. The results from Bott's flux method [15] are almost identical to those of Simmel et al. [24].

number and mass into bin k and bin $k + 1$ are not derived directly from the gain integrals according to the moment equations.

The mass density distributions at $t = 20$ min and $t = 40$ min are shown in Figs. 6 and 7, respectively, on a linear-linear plot for different numerical approaches. The bin resolution is set to $s = 2$. Figs. 6 and 7 indicate that BIMGQ provides the best prediction near the peak region, compared to other approaches. Overall, BIMGQ and BRM are more accurate than LFM and LDM, especially near the peak of the distribution. The LDM appears to give the worst prediction near the peak.

Fig. 8 compares four numerical methods at $t = 20$ min and $t = 40$ min on a log–log plot. This figure allows a closer inspection of the right tail of the drop size spectra. B-R's method gives almost exact prediction of the distribution in the tail region. BIMGQ very slightly underestimates the mass density in the tail region. Simmel's linear discrete method and Bott's linear flux method both overestimate the mass density due to numerical diffusion. Bott's LFM appears to yield the worst prediction in the tail region.

3.2. Hydrodynamic kernels

Next we consider two hydrodynamic kernels, the Long kernel [13] and the Hall kernel [14] often used along with KCE to study the growth of cloud droplets due to gravitational collision-coalescence. The Long kernel is based on the gravitational coalescence with empirical curve fittings to the collision efficiency. The Hall kernel uses tabulated data of collision efficiency in [14]. A detailed description of these kernels along with the model for terminal velocity can be found in [12]. These hydrodynamic kernels are highly nonlinear and can lead to explosive growth of the size spectrum [4]. In the following, the same initial condition and parameter settings as stated previously are assumed.

In this paper, we focus on numerical issues related to the size discretization of the kinetic collection equation. The time step dt is fixed to a small value of 1 s, so that the time discretization error is negligible even for hydrodynamic kernels. To confirm this, we fix the size resolution parameter to $s = 16$ in BIMGQ so the size discretization error is negligible (see below for confirmation of this). We vary the time step size, and compare the resulting moments at $t = 60$ min. We found that the first four moments are almost identical (with relative error less than 1%) when $dt \leqslant 2$ s.

Because analytical solutions are not available for these hydrodynamic kernels, we shall first establish a benchmark numerical solution so that the accuracy of different numerical approaches can be assessed. We first
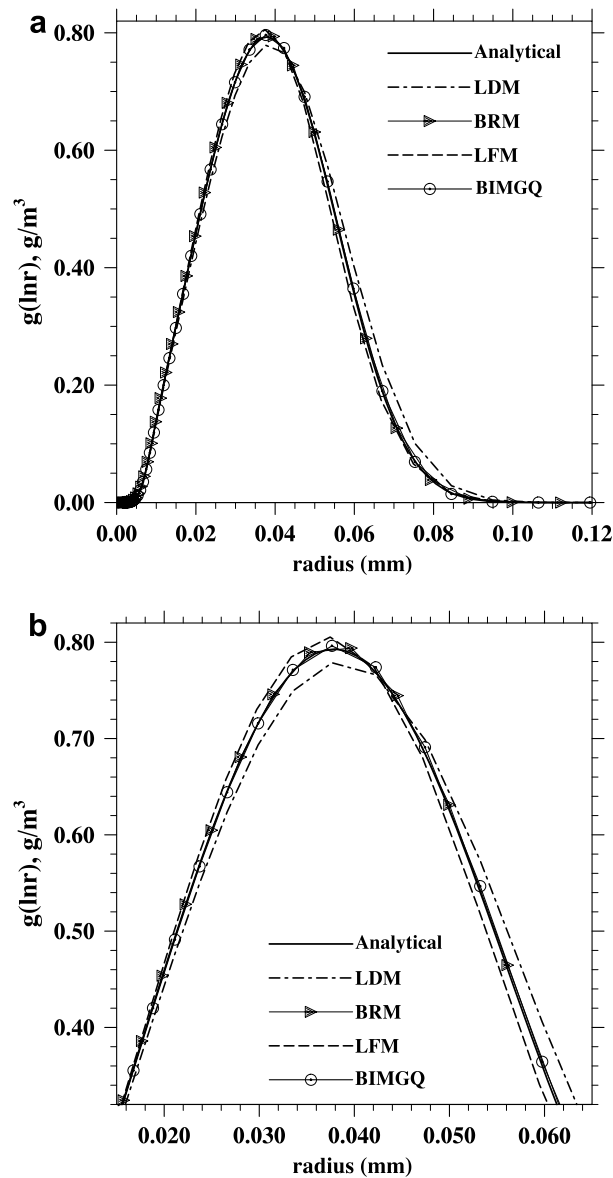
Fig. 6. Mass density for Golovin kernel as a function of droplet size at $t = 20$ min. Numerical solutions from different approaches are compared with the analytical solution: (a) the full size range; (b) region near the peak.

ran BIMGQ along with BRM, LDM, and LFM for a pure collision-coalescence system governed by the Long kernel, starting with a coarse bin grid at $s = 1$. As the grid is gradually refined with $s = 2, 4, 8$, and $+16$, we found that the solutions based on BIMGQ, BRM, and LDM all converge to the same solution at all times up to $t = 3600$ s. Fig. 9 displays the solution at 7 different times obtained with $s = 16$, noting that each of the 7 curves actually contains three independent curves based on BIMGQ, BRM, and LDM. Because the results from the three methods overlap precisely, they cannot be distinguished in Fig. 9, with a minor exception at $t = 30$ min when a slight difference is seen at the far end of the steep advancing front with $g < 10^{-7}$ g/m^3. This minor difference appears to be related to the transition from the autoconversion growth mode to the accretion mode [4], but disappears almost completely a few minutes later. To the authors' knowledge, no such benchmark solution at this fine resolution has been documented simultaneously with three independent methods. Specifically, we were able to modify the BRM code to allow for the use of arbitrary s. Most previously published results of the BRM code used only one bin resolution at $s = 2$. The distributions shown in Fig. 9 can be viewed
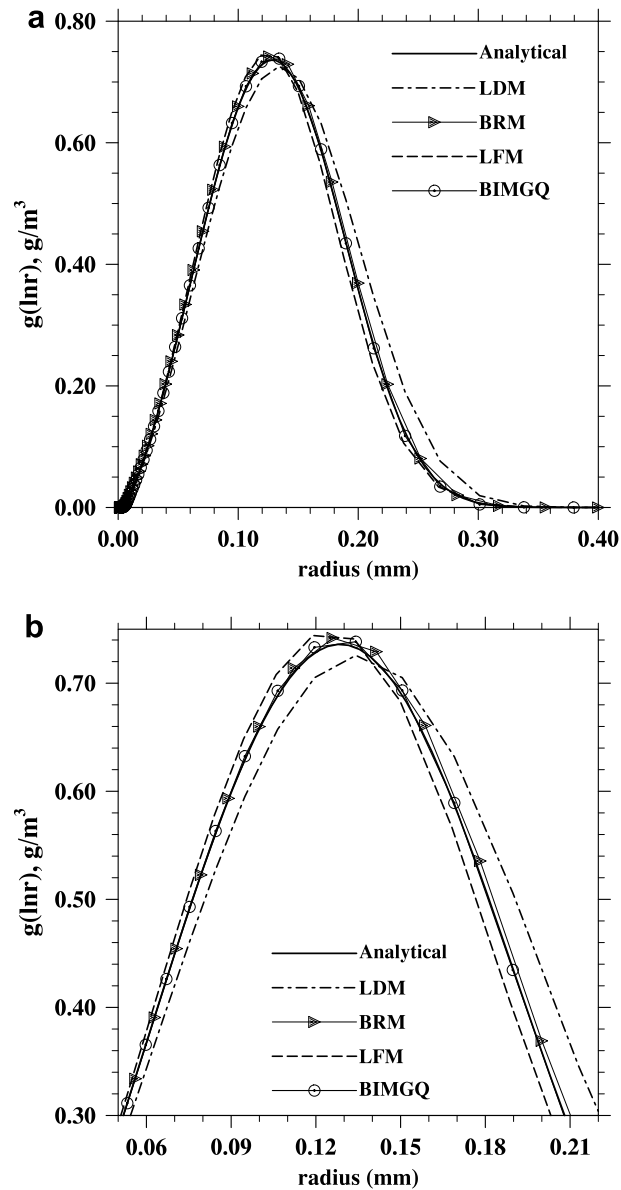
Fig. 7. Mass density for Golovin kernel as a function of droplet size at $t = 40$ min. Numerical solutions from different approaches are compared with the analytical solution: (a) the full size range; (b) region near the peak.

as the ground-truth solution of the KCE for pure collision-coalescence governed by the highly nonlinear Long kernel. The LFM overpredicts the distribution at the steep front and fails to converge even for $s = 32$.

The time evolution of the size distribution clearly shows two distinct stages. For $t < 20$ min, the growth is governed by collisions of small cloud droplets near the initial peak to slowly feed the mass to the nearby front at the right, gradually building up the mass around 50 μm in radius. The evolution in this early stage is called autoconversion by Berry and Reinhardt [4], this process proceeds very slowly since the collection kernel is small in magnitude. Once a small percentage of droplets larger than 50 μm has developed, the larger cross-collision collection kernel between these larger droplets and the small cloud droplets at the initial peak converts much more effectively the mass from the initial peak to droplets near the advancing front, leading to the generation of a second peak that moves continuously and rapidly to the right, due to the ever increasing collection kernel for cross-size collisions. This process initiates the accretion mode of growth in which the mass from the initial peak converts directly to the second peak. On the log–log plot, a somewhat discontinuous minimum at
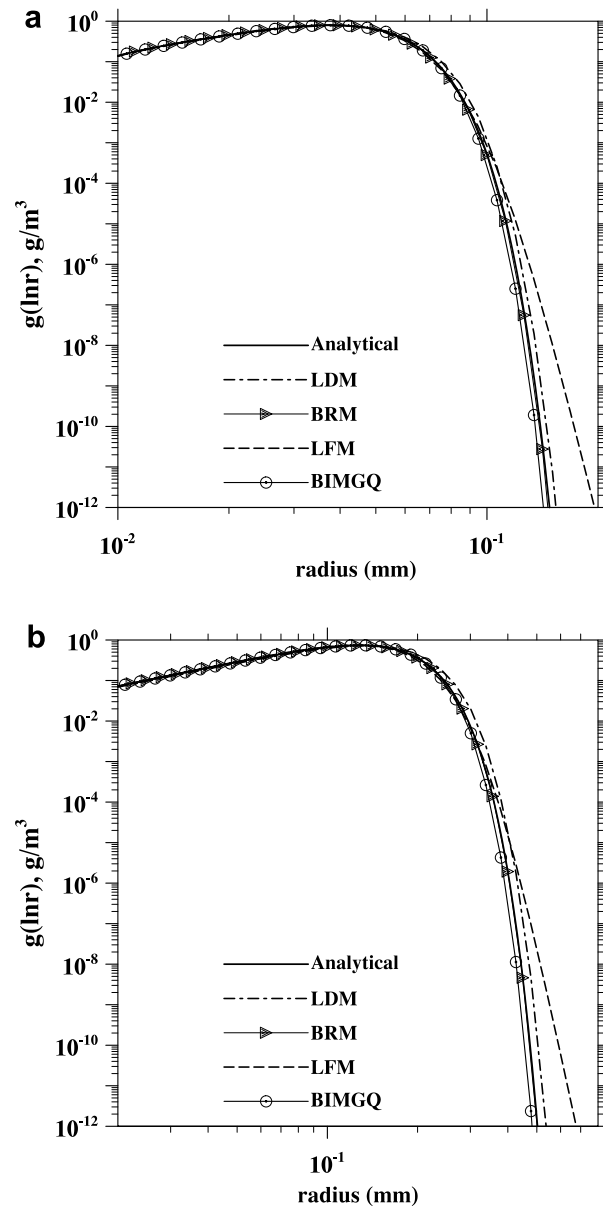
Fig. 8. Logarithmic plots of mass density for Golovin kernel as a function of droplet size: (a) $t = 20$ min and (b) $t = 40$ min. Numerical solutions at the bin resolution $s = 2$ from different approaches are compared with the analytical solution.

$r = 51$ μm can be observed for the Long kernel. This is perhaps due the somewhat non-smooth transition of collision efficiency from less than one for $r < 50$ μm to one for $r > 50$ μm.

Another check of the convergence is to compute the moments $M_p(t)$ from these fine-resolution numerical solutions, which are shown in Table 3 for $k = 0$ (number) and 1 (mass), and in Table 4 for $k = 2$ (radar reflectivity) and 3. The moments are calculated based on the mass density distribution using Eq. (48). By design, the first moment (mass density) is exactly conserved in BIMGQ, LDM, and LFM, while an extremely small increase in mass (with no physical significance) is observed in BRM. BIMGQ provides a number density identical to BRM at all times. The maximum errors in number density for LDM and LFM, when compared with BRM, occur at later times and are 0.9% and 1.8%, respectively. Of significance is the fact that the total number density changes slowly before the first 30 minutes but then drops very quickly in the last 30 minutes. Physically, this is due to the strong nonlinearity of the collection kernel which makes it possible for the system to
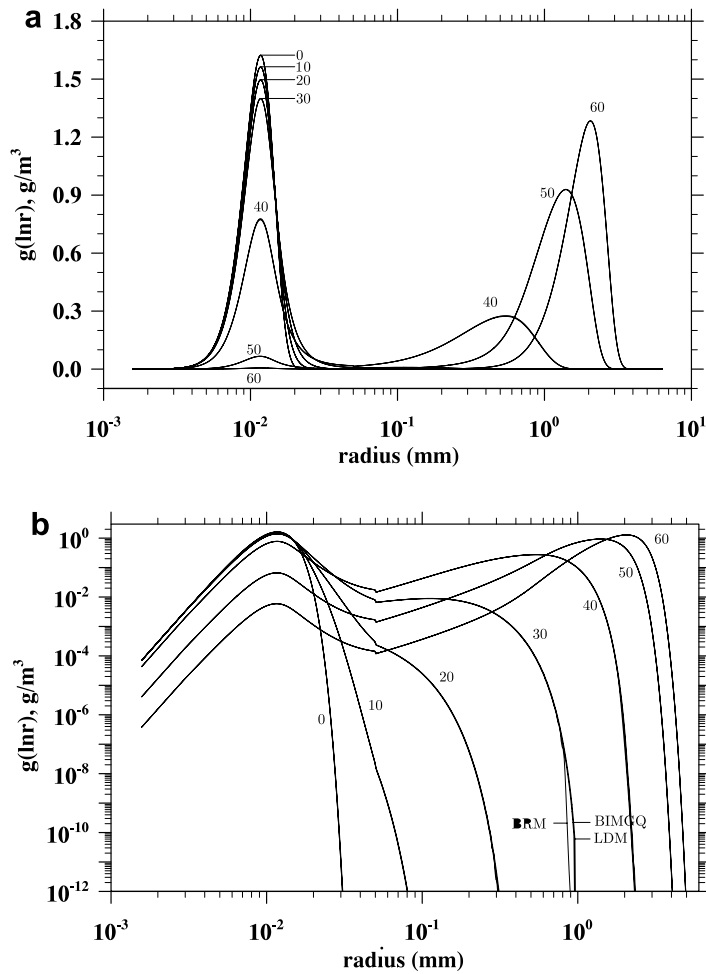
Fig. 9. The converged solutions of the mass density distribution for the Long kernel: (a) log-linear plot; (b) log–log plot. The number marks the time in minutes. Each line represents actually three overlapping lines from the three methods (BIMGQ, BRM, LDM) unless explicitly noted for the steep front at $t = 30$ min. shown in (b). A fine bin resolution with $s = 16$ is used for all methods.

switch from the autoconversion growth mode of small cloud droplets to the accretion of small cloud droplets by newly formed rain drops.

Given the high accuracy of BRM and the above demonstrated convergence, we may take the solution of BRM at $s = 16$ as the *exact* solution. The second and third order moments, $M_2(t)$ and $M_3(t)$, obtained from the other three methods at $s = 16$ can now be compared to these from BRM. BIMGQ gives essentially identical values for $M_2(t)$ and $M_3(t)$ as BRM, with relative difference less than 0.2%. LDM has a maximum relative error of 3.3% for $M_2(t)$ and 5.7% for $M_3(t)$; it is interesting to note that the relative errors reach the maximum at about $t = 30$ min and then decrease afterwards. Because of the overprediction at the steep front, LFM has a maximum relative error of 9.8% for $M_2(t)$ and 29.8% for $M_3(t)$. A small overprediction can have a noticeable effect on high order moments. The difficulty for Bott's LFM to converge and the large errors for high-order moments imply some inherent inconsistency of the approach. The first four moments listed in Tables 3 and 4 from BRM and BIMGQ can be viewed as exact benchmark values against which the accuracy of any numerical method for solving KCE can be evaluated. The above also indicates that a visual overlap of the curves does not guarantee the convergence of high-order moments. On the other hand, a very small difference in the far tail does not necessarily imply a poor prediction of a particular moment.

A similar task was undertaken to establish the benchmark solution for the Hall kernel. Again at $s = 16$, BIMGQ, BRM, and LDM converge essentially to a same solution at all times, as shown in Fig. 10. The overall

Table 3
Predicted total system mass and number densities for a system driven by the Long kernel

t (min)	$M_0(t)$ (1/cm^3)				$M_1(t)$ (g/m^3)			
	BIMGQ	BRM	LDM	LFM	BIMGQ	BRM	LDM	LFM
0	295.4	295.4	295.4	295.4	0.999989	0.999989	0.999989	0.999989
10	287.4	287.4	287.4	287.4	0.999989	0.999990	0.999989	0.999989
20	278.4	278.4	278.4	278.3	0.999989	0.999991	0.999989	0.999989
30	264.4	264.4	264.4	264.3	0.999989	0.999999	0.999989	0.999989
40	151.7	151.7	150.8	150.4	0.999989	1.00003	0.999989	0.999989
50	13.41	13.41	13.29	13.41	0.999989	1.00003	0.999989	0.999989
60	1.212	1.212	1.203	1.234	0.999989	1.00004	0.999989	0.999989

A fine resolution at $s = 16$ was used for all methods.

Table 4
Predicted second and third moments for a system driven by the Long kernel

t (min)	$M_2(t)$ (mg^2/cm^3)				$M_3(t)$ (mg^3/cm^3)			
	BIMGQ	BRM	LDM	LFM	BIMGQ	BRM	LDM	LFM
0	6.739E−9	6.740E−9	6.739E−9	6.739E−9	6.813e−14	6.818e−14	6.813e−14	6.813e−14
10	7.402E−9	7.402E−9	7.402E−9	7.402E−9	9.305e−14	9.309e−14	9.305e−14	9.305e−14
20	8.720E−9	8.720E−9	8.724E−9	8.726E−9	5.710e−13	5.717e−13	5.904e−13	6.324e−13
30	3.132E−7	3.132E−7	3.234E−7	3.440E−7	3.967e−8	3.967e−8	4.193e−8	5.148e−8
40	3.498e−4	3.499e−4	3.589e−4	3.844e−4	1.048e−3	1.049e−3	1.093e−3	1.288e−3
50	1.068e−2	1.068e−2	1.078e−2	1.119e−2	2.542e−1	2.545e−1	2.588e−1	2.806e−1
60	3.199e−2	3.200e−2	3.212e−2	3.275e−2	1.731	1.733	1.744	1.815

A fine resolution at $s = 16$ was used for all methods.

growth rate for the Hall kernel is slower than that for the Long kernel. Another noticeable difference between results of the Hall kernel and Long kernel lies in the small size range. The mass density for droplets below 10 μm decreases more quickly and uniformly in the case of Long kernel (Fig. 9b), but this is not observed for the Hall kernel (Fig. 10b). LFM also fails to converge for the case of Hall kernel.

The moments from various methods at $s = 16$ are provided in Tables 5 and 6. Once again, BIMGQ and BRM produce almost identical first four moments at all times, with a relative difference less than 0.2%. Having two different classes of numerical methods providing the identical solution confirms the convergence. The maximum relative errors for LDM are 0.16%, 1.6%, 3% for $M_0(t)$, $M_2(t)$, and $M_3(t)$, respectively. LFM has maximum relative errors of 0.31%, 5.0%, 14.6% for $M_0(t)$, $M_2(t)$, and $M_3(t)$, respectively. The benchmark values for these moments can be taken from either BIMGQ and BRM. In the rest of this paper, the ground-truth solution for $g(x,t)$ shall be taken as the BRM solution at $s = 16$.

Next, we shall compare the numerical solutions at the intermediate bin resolution of $s = 2$. Fig. 11 shows the results at $t = 20$ min. BRM and BIMGQ are closer to the converged solution, especially near the peak region. Fig. 12 shows the results at $t = 40$ min. At this time, the mass density function exhibits two peaks. BRM provides the best solution not only at the first peak but also at the second peak. BIMGQ overestimates the distribution at the first peak and Bott's LFM and Simmel's LDM underestimate it at the first peak. In Fig. 13, the results are replotted on logarithmic scales. At the bin resolution of $s = 2$, BRM provides the most accurate result when compared to the converged solution. For the region near the steep advancing front, all methods except BRM fail to provide a satisfactory solution at this bin resolution. Similar observations can be made for the case of the Hall kernel. While BIMGQ with $s = 2$ works well for the Golovin kernel, the linear prescription for the binwise distribution is inadequate at $s = 2$ for the case of strongly nonlinear hydrodynamic kernels. However, we will demonstrate later that BIMGQ improves significantly when the bin resolution is doubled by setting $s = 4$, i.e., the method has a rapid and consistent convergence rate. Alternatively, we may consider the use of a different local approximation such as a power-law nonlinear distribution. This possibility will be studied in a subsequent paper.

3.3. Numerical accuracy and convergen

Due to the approximations in evaluating ... loss integrals associated with the discretizati... time and droplet size, two important issues, ... ccuracy and efficiency, must be ...

Table 6
Predicted second and third moments for a system driven by the Hall kernel

t (min)	$M_2(t)$ (mg^2/cm^3)				$M_3(t)$ (mg^3/cm^3)			
	BIMGQ	BRM	LDM	LFM	BIMGQ	BRM	LDM	LFM
0	6.739e−9	6.740e−9	6.739E−9	6.739E−9	6.813e−14	6.818e−14	6.813e−14	6.813e−14
10	7.184e−9	7.185e−9	7.183e−9	7.184e−9	8.282e−14	8.286e−14	8.282e−14	8.283e−14
20	7.999e−9	7.999e−9	8.001e−9	8.002e−9	3.801e−13	3.798e−13	3.855e−13	3.964e−13
30	7.827e−8	7.815e−8	7.941e−8	8.194e−8	2.531e−9	2.531e−9	2.606e−9	2.901e−9
40	1.942e−5	1.939e−5	1.966e−5	2.035e−5	6.107e−6	6.100e−6	6.226e−6	6.716e−6
50	7.928e−4	7.915e−4	7.983e−4	8.221e−4	2.108e−3	2.103e−3	2.137e−3	2.285e−3
60	6.997e−3	6.989e−3	7.025e−3	7.163e−3	1.221e−1	1.219e−1	1.231e−1	1.283e−1
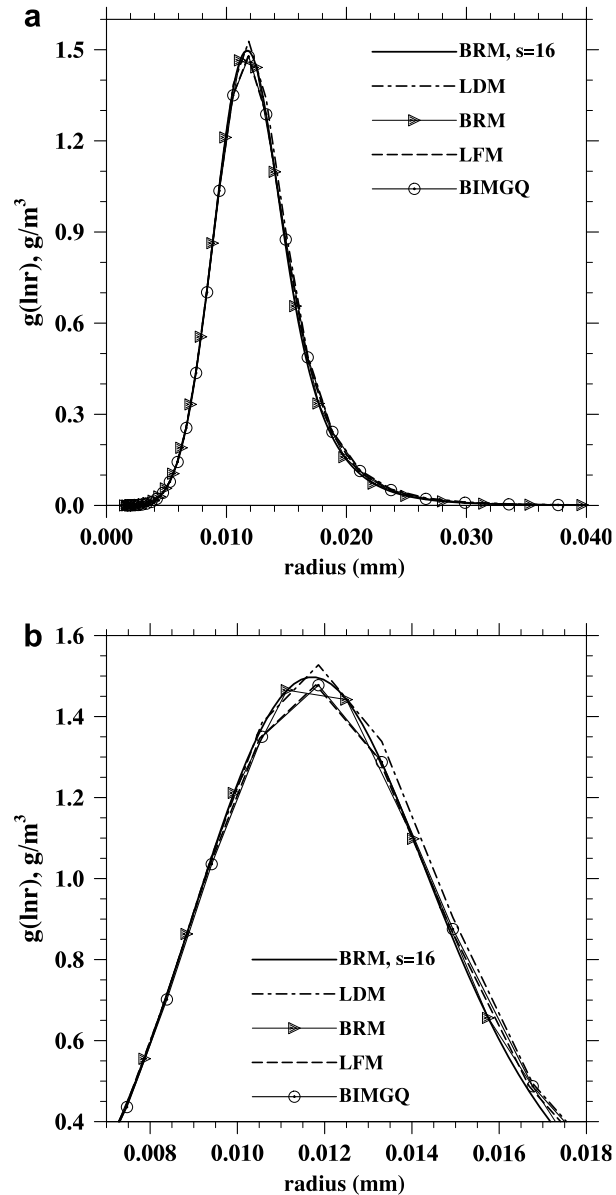
Fig. 11. Mass density for the Long kernel as a function of droplet size at $t = 20$ min. Numerical solutions at $s = 2$ from different methods are compared with BRM solution at $s = 16$.
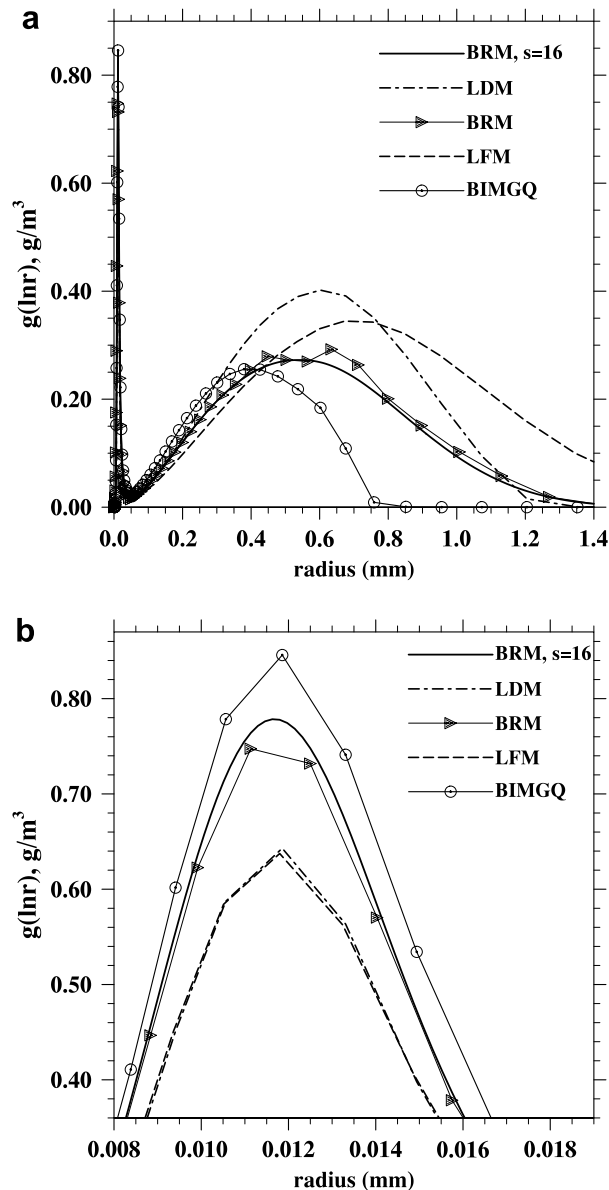
Fig. 12. Mass density changing for the Long kernel as a function of droplet size at $t = 40$ min. Numerical solutions at $s = 2$ from different methods are compared with BRM solution at $s = 16$.

numerical method for solving KCE. The numerical accuracy concerns the difference between a numerical solution of KCE and the converged solution of KCE. It may be measured at several levels, ranging from the overall mass conservation over time (an integral property that must be satisfied) to the instantaneous distribution of droplet number density. In many cases, while the overall mass conservation is ensured by design, the instantaneous distribution may deviate from the converged solution due to numerical diffusion and dispersion.

Here we develop quantitative measures to rigorously examine the accuracy and convergence properties of BIMGQ for both the Golovin kernel and hydrodynamic kernels. The rate of convergence of a given algorithm is an important measure of the consistency and quality of the algorithm.

It is usually expected that a higher bin resolution would provide a more accurate representation but at the same time require a longer computational time. In Figs. 14–16, we compare the instantaneous mass distributions obtained with different bin resolutions. For the case of Golovin kernel (Fig. 14), they are compared also

with the analytical solution. For the cases of the and the Hall kernels (Fig. 15 and 16), the benchmark converged solution (BRM at $s = 16$) is used to ass e rate of convergence as the bin resolution is increased. Clearly, BIMGQ converge to the true solution in all es when the bin resolution is increased. For the case of Golovin kernel, when the bin resolution measured b the parameter s is 2 or higher, BIMGQ essentially recover the analytical solution not only for early time ($t = 20\,\text{min}$) but also for the later time ($t = 40\,\text{min}$). When the hydrodynamic kernels are considered, we find that BIMGQ requires a bin resolution of $s = 4$ to provide a solution of good quality.

To quantify the accuracy of different numerical methods for solving KCE, we introduce the moments of the size distribution calculated numerically as
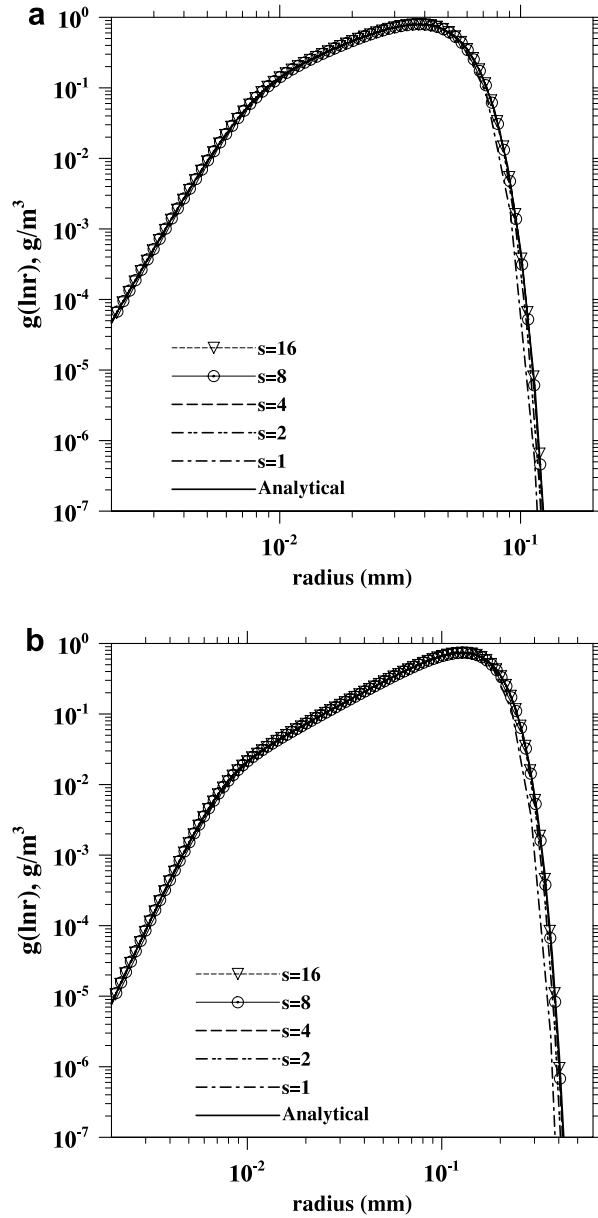
Fig. 14. The instantaneous mass density distributions obtained with BIMGQ at different bin resolutions for the Golovin kernel: (a) $t = 20$ min; (b) $t = 40$ min. Note that not all the data points are plotted for $s = 8$ and $s = 16$ in order to avoid clustering of symbols.

$$M_k(t;s) = \int n(x;s)x^k \, \mathrm{d}x = \int g(\ln r;s)x^{k-1} \, \mathrm{d}(\ln r) \equiv \sum_i g(t;i,s)(x_i\sqrt{\rho})^{k-1}\frac{\ln \rho}{3}, \quad k = 0, 1, 2, 3, \tag{48}$$

where the geometric average, $x_i\sqrt{\rho}$, of x_i and x_{i+1} is used in the above expression to observe that the integration is performed on the logarithmic axis. The above definition only makes use of the computed mass in the bins so it did not take the full advantage of the two degrees of freedom available in BIMGQ. This is so defined to allow for the evaluation of moments in Bott's LFM for which only one moment (the bin mass) is explicitly employed. The relative error for the kth-order moment is defined as
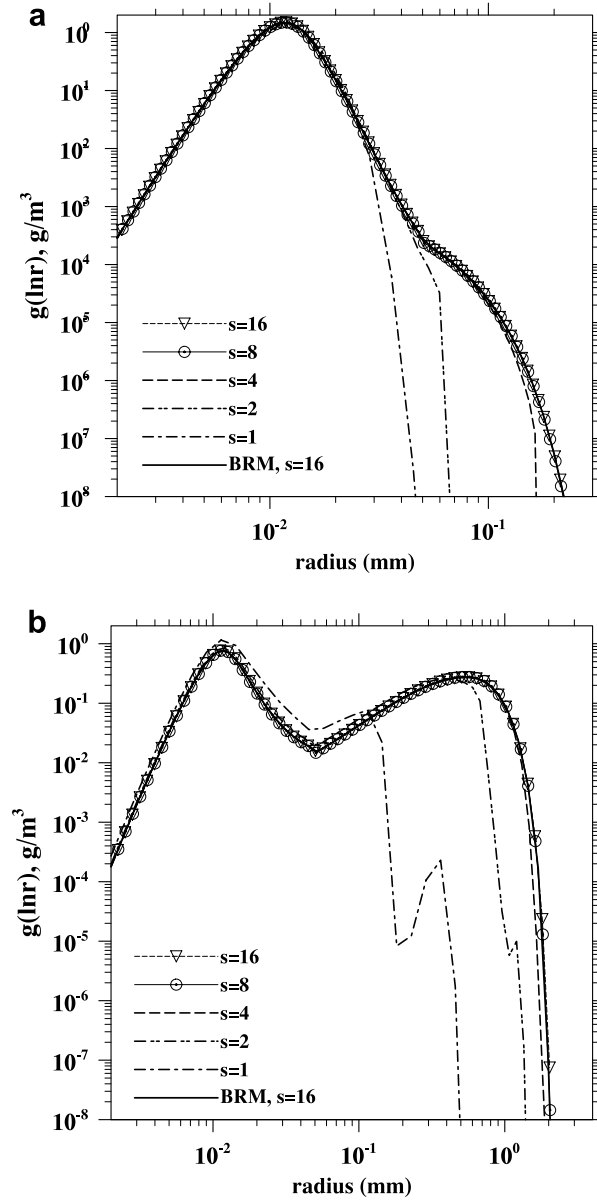
Fig. 15. The instantaneous mass density distributions obtained with BIMGQ at different bin resolutions for the Long kernel: (a) $t = 20$ min; (b) $t = 40$ min.

$$\epsilon_k(t;s) = \frac{|M_k(t;s) - M_k(t;C)|}{M_k(t;C)}, \tag{49}$$

where $M_k(t;C)$ is the converged numerical benchmark discussed previously. For the Golovin kernel, the benchmark is set to be $M_k(t;32)$ calculated from the BIMGQ code. Here, the analytical solution is not used due to the small mass truncation below x_1 and above x_{M+1}. For the Long kernel and Hall kernel, the benchmark is $M_k(t;16)$ obtained from BRM. Fig. 17 shows the relative errors of different methods when predicting the first four moments for the case of Golovin kernel at $t = 40$ min. BIMGQ has a better accuracy for all moments than LFM and LDM. For the zeroth moment, the relative error for BIMGQ is about one order less than those of LFM and LDM. For higher order moments ($k = 2$ and 3), BIMGQ could be two to three orders more accurate than LFM and LDM at high resolutions. For unclear reason, LFM has a larger error at $s = 16$

than that at $s = 8$, while in all other methods the relative errors decrease monotonically as the bin resolution parameter s
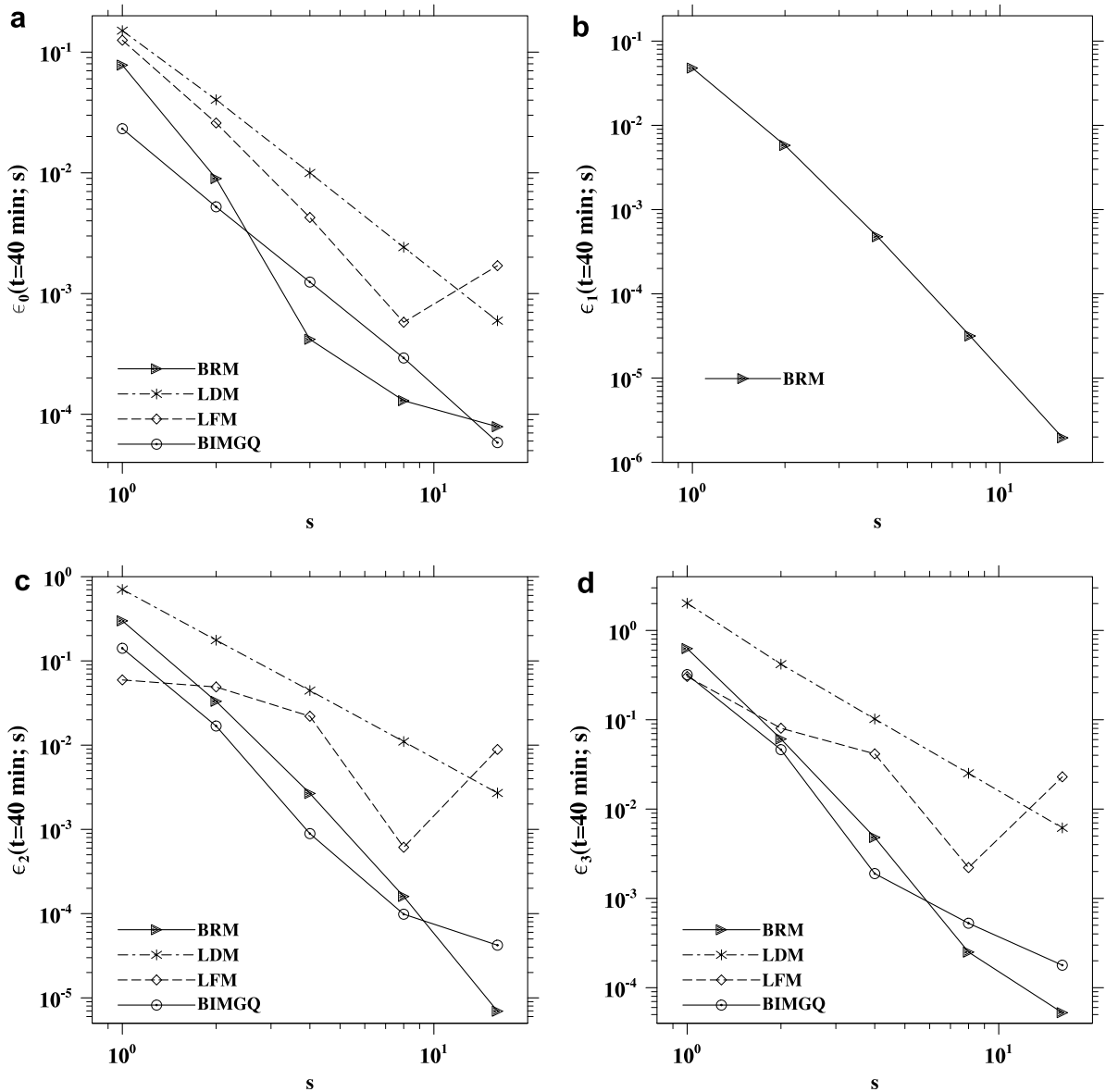
Fig. 17. Relative error in the predicted moments for the case of Golovin kernel at $t = 40$ min: (a) zeroth moment or the number density; (b) first moment or mass, here only BRM is considered as other methods have no error by design; (c) second moment; (d) third moment.

$s = 16$, BIMGQ is clearly more accurate than LFM and LDM. BRM could cause an overprediction of system mass by 4% at $s = 1$ after 40 min, although this problem can be neglected for $s \geqslant 2$. Very similar trends are found for case of the Long kernel.

Finally, we briefly compare the CPU times needed for different methods in Fig. 19. All runs are performed on a PC linux workstation with a 2.8 GHz Pentium processor. The CPU times are for runs with 3600 time steps and d$t = 1$ s. The CPU time scales roughly with s^2, which is expected as the number of operations is proportional to the number of pair interactions. LDM requires the shortest CPU. The BRM code has been highly optimized over the years and is the next efficient code in terms of CPU. The CPU times of BIMGQ and LFM are comparable. Since our code has not been fully optimized at this stage, it is believed that a significant speedup is still possible for BIMGQ.
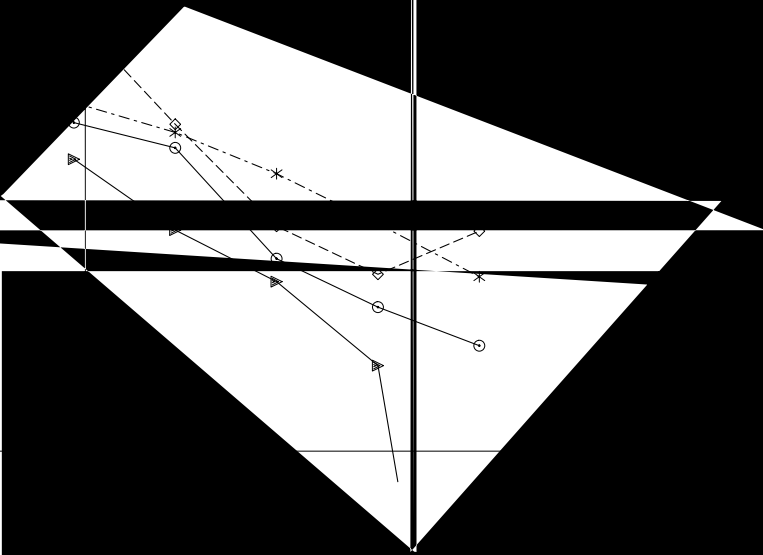
Summ

A ne
collectio
the hum
resentat
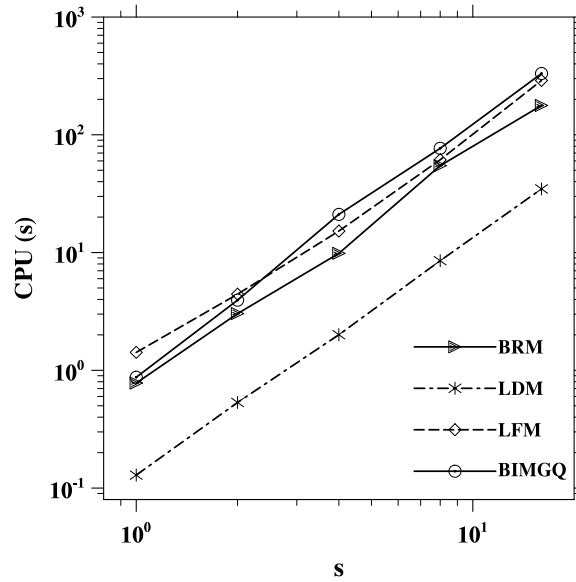momen
of sour
possibly
se ation
h ndled exac

Fig. 19. CPU time for different methods for the case of Hall kernel. Time interval d*t* is 1 s and total simulation time is 60 min.

complex deductions. In essence the method combines favorable features in previous spectral moment-based and bin-based pair-interaction (or flux) methods to greatly enhance the logic, consistency, and simplicity in the numerical method and its implementation. The method represents an improvement over the linear flux method (LFM) of Bott [15] and the linear discrete method (LDM) of Simmel et al. [24].

The accuracy and convergence of BIMGQ are examined along with three other methods, the method of Berry and Reinhardt (BRM; [4]), the linear flux method (LFM) of Bott [15], and the linear discrete method (LDM) of Simmel et al. [24]. For the case of the Golovin kernel, it is shown that our method predicts exactly both the overall number density and mass density, regardless of the bin resolution used; and the instantaneous mass distribution can be accurately produced at a moderate bin resolution of $s = 2$. For the two hydrodynamic kernels (the Long kernel and the Hall kernel), it is shown that BIMGQ, BRM, and LDM are capable of generating the ground-truth converged solution at a bin mass ratio of $2^{1/16} = 1.04427$. The converged values of the first four moments for each hydrodynamic kernel have been presented for the first time. It is hoped that both the converged mass distributions and moments for the two hydrodynamic kernels can be used as the benchmark to measure the accuracy of any numerical method for KCE in the future. Numerical solutions of good quality can be obtained with BIMGQ at $s = 4$ for the hydrodynamic kernels.

Quantitative measures are developed to quantify the accuracy and convergence properties of the different methods. A monotonic convergence has been demonstrated for BIMGQ, BRM, and LDM, but not for LFM. It is shown that BIMGQ has a superior accuracy for the Golovin kernel and a monotonic convergence behavior for hydrodynamic kernels. Overall, BRM and BIMGQ have similar convergence rates for the Golovin kernel. For the case of hydrodynamic kernels, BRM is the most accurate method for moderate bin resolution ($s = 2$) due to the high-order Lagrangian interpolations used for both the mass distribution and the collection kernel; and BIMGQ is more accurate than LDM and LFM, especially when high-order moments are concerned. The convergence measure developed here should be of value to future studies on numerical solution of KCE.

For all the three collection kernels tested in this paper, BIMGQ at low bin resolutions tends to underpredict the mass distribution at the steep advancing front, unlike the overprediction observed for LFM and LDM. This may be viewed as an indication that the method exhibits very little numerical diffusion. This underprediction may be explained as follows. The linear binwise representation tends to yield a partial linear distribution at the left bin boundary (scenario (b) in Fig. 3) when applied to the bins near the steep advancing front, as the distribution there falls exponentially. As a result, it slows down rather than promotes the growth in the steep tail region. This also explains why the underprediction becomes most obvious for the lowest resolution

at $s = 1$. We view this slower growth at coarse bin resolutions as a desirable feature since the method itself would not broaden the size spectrum just because of numerical errors, while most existing numerical methods for KCE tend to behave in the opposite way leading to artificially fast growth. It is also important to note that the level of approximation in representing the collection kernel can influence the rate of growth. For example, the less accurate Long kernel yields a faster growth than the more accurate Hall kernel. This is another reason why a slower growth at coarser bin resolution is more desirable.

We recognize that the number of variables solved in BIMGQ and LDM are roughly twice the number of variables solved in BRM and LFM. In dynamic cloud models, this could imply twice of dynamic equations need to be solved in BIMGQ and LDM (thus twice the CPU time as well). A fair comparison would be between the results of BIMGQ and LDM at a given s with those of BRM and LFM at $2s$. The convergence plots, Figs. 17 and 18, do contain the information that allows the comparison based on the number of variables used. In this sense, LFM is quite efficient and reasonably accurate and BRM is the most accurate of all.

The main utility of the BIMGQ method demonstrated in this paper is the establishment of benchmark solution for any collection kernel. Another utility of the method is demonstrated in Xue et al. [40] in which the method is applied to study how the growth process depends on the turbulent enhancement of the collision kernel. The accuracy of the method allows us to focus on the effects of the kernel and the width of the initial size distribution, instead of worrying about numerical integration errors.

Finally, this paper represents merely a first step in bridging the spectral moment methods and pair-interaction flux methods. The technique developed here can be made more accurate for low to moderate bin resolutions ($s = 1$ and 2), if a more general, power-law distribution is used to describe the number density distribution in each bin. However, the linear representation used here has the advantage of simplicity and ease to evaluate the gain and loss integrals by Gauss quadrature. A power-law distribution would be more appropriate for regions of large local gradients, such as near the advancing steep front. It is also possible to use a linear representation in most regions and a power-law representation for selected regions to obtain an optimal representation in terms of accuracy and efficiency. In principle, the method can be used for a combination of uniform grid and geometric grid or arbitrary bin grid, but with the complication that the target due to a pair interaction may contain more than two bins. Some of these possibilities will be explored in future investigations.

References

[1] M. von Smoluchowski, Versuch einer mathematischen Theorie der Koagulationskinetic kolloider Losunggen, Z. Physik. Chem. 92 (1917) 129.

[2] H.R. Pruppacher, J.D. Klett, Microphysics of Clouds and Precipitation, second ed., Kluwer Academic Publishers, Boston, 1997, p. 954.

[3] J.H. Seinfeld, S.N. Pandis, Atmospheric Chemistry and Physics: From Air Pollution to Climate Change, Wiley, New York, 1997.

[4] E.X. Berry, R.L. Reinhardt, An analysis of cloud drop growth by collection: Part 1. Double distribution, J. Atmos. Sci. 31 (1974) 1814–1824.

[5] D. Aldous, Deterministic and stochastic models for coalescence (aggregation and coagulation): a review of the mean-field theory for probabilists, Bernoulli 5 (1999) 3–48.

[6] M. Smoluchowski, Drei Vorträge über diffusion, brownsche bewegung und koagulation von kolloidteilchen, Phys. Z. 17 (1916) 557–585.

[7] T. Schumann, Theoretical aspects of the size distribution of fog particles, Q. J. R. Meteorol. Soc. 66 (1940) 195–207.

[8] J. Mcleod, On an infinite set of nonlinear differential equations, Quart. J. Math. Oxford 13 (1962) 119–128.

[9] A.M. Golovin, The solution of the coagulation equation for cloud droplets in a rising air current, Izv. Zkad. Nauk. SSSR Ser. Geofiz. 5 (1963) 873.

[10] W.T. Scott, Analytical studies of cloud droplet coalescence, J. Atmos. Sci. 25 (1968) 54.

[11] J.D. Klett, Class of solultion to steady-state, source-enhanced, kinetic coagulation equation, J. Atmos. Sci. 32 (1975) 380–389.

[12] Y. Xue, Effects of air turbulence and stochastic coalescence on the size distribution of cloud droplets, Ph.D. Dissertation, University of Delaware, 214 pages, AAT 3221090, ISBN 0542724770, Available from ProQuest Information and Learning Company, Ann Arbor, MI, USA (ProQuest document ID: 1172112611).

[13] A.B. Long, Solutions to the droplet coalescence equation for polynomial kernels, J. Atmos. Sci. 11 (1974) 1040–1052.

[14] W.D. Hall, A detailed microphysical model with a two-dimensional dynamic framework: model description and preliminary results, J. Atmos. Sci. 37 (1980) 2486–2507.

[15] A. Bott, A flux method for the numerical solution of the stochastic collection equation, J. Atmos. Sci. 55 (1998) 2284–2293.

[16] S. Tzivion, T.G. Reisin, Z. Levin, A numerical solution of the kinetic collection equation using high spectral grid solution: a proposed reference, J. Comput. Phys. 148 (1999) 527–544.

[17] F. Gelbard, J.H. Seinfeld, Numerical solution of the dynamic equation for particulate systems, J. Comput. Phys. 28 (1978) 357.

[18] D. Eyre, C.J. Wright, G. Reuter, Spline-collocation with adaptive mesh scheme grading for solving the stochastic collection equation, J. Comput. Phys. 78 (1988) 288–304.

[19] G.G. Carrio, L. Levi, On the parameterization of autoconversion. Effects of small-scale turbulent motions, Atmos. Res 38 (1995) 21–27.

[20] R. Bleck, A fast approximate method for integrating the stochastic coalescence equation, J. Geophys. Res. 75 (1970) 5165–5171.

[21] I.M. Enukashvily, A numerical method for integrating the kinetic equation of coalescence and breakup of cloud droplets, J. Atmos. Sci. 37 (1980) 2521–2534.

[22] S. Tzivion, G. Feingold, Z. Levin, An efficient numerical solution to the stochastic collection equation, J. Atmos. Sci. 44 (1987) 3139.

[23] S. Tzivion, T.G. Reisin, Z. Levin, A new formulation of the spectral multi-moment method for calculating the kinetic collection equation: more accuracy with few bins, J. Comput. Phys. 171 (2001) 418.

[24] M. Simmel, T. Trautmann, G. Tetzlaff, Numerical solution of the stochastic collection equation – comparison of the linear discrete method with other methods, Atmos. Res. 61 (2002) 135–148.

[25] A. Kovetz, B. Olund, The effect of coalescence and condensation on rain formation in a cloud of finite vertical extent, J. Atmos. Sci. 26 (1969) 1060–1065.

[26] M.J. Hounslow, R.L. Ryall, V.R. Marshall, A discretized population balance for nucleation growth and aggregation, AIChE J. 34 (1988) 1821–1832.

[27] S. Kumar, D. Ramkrishna, On the solution of population balance equations by discretization – I. A fixed pivot technique, Chem. Engi. Sci. 51 (1996) 1311–1332.

[28] S. Kumar, D. Ramkrishna, On the solution of population balance equations by discretization – II. A moving pivot technique, Chem. Engi. Sci. 51 (1996) 1333–1342.

[29] S. Kumar, D. Ramkrishna, On the solution of population balance equations by discretization – III. Nucleation, growth and aggregation of particles, Chem. Engi. Sci. 52 (1997) 4659–4679.

[30] L.P. Wang, O. Ayala, S.E. Kasprzak, W.W. Grabowski, Theoretical formulation of collision rate and collision efficiency of hydrodynamically-interacting cloud droplets in turbulent atmospheres, J. Atmos. Sci. 62 (2005) 2433–2450.

[31] N. Riemer, A.S. Wexler, Droplets to drops by turbulent coagulation, J. Atmos. Sci. 62 (2005) 1962–1975.

[32] L.P. Wang, O. Ayala, Y. Xue, W.W. Grabowski, Comments on droplets to drops by turbulent coagulation, J. Atmos. Sci. 63 (2006) 2397–2401.

[33] N. Riemer, A.S. Wexler, Comments on droplets to drops by turbulent coagulation – Reply, J. Atmos. Sci. 63 (2006) 2402–2404.

[34] J.W. Telford, A new aspect of coalescence theory, J. Meteorol. 12 (1955) 436–444.

[35] D.T. Gillespie, The stochastic coalescence model for cloud droplet growth, J. Atmos. Sci. 29 (1972) 1496.

[36] A.B. Kostinski, R.A. Shaw, Fluctuations and luck in droplet growth by coalescence, Bull. Am. Meteorol. Soc. 86 (2005) 235–244.

[37] I.A. Valioulis, E.J. List, A numerical evaluation of the stochastic completeness of the kinetic coagulation equation, J. Atmos. Sci. 41 (1984) 2516.

[38] L.P. Wang, O. Ayala, Y. Xue, W.W. Grabowski, Effects of stochastic coalescence and air turbulence on the size distribution of cloud droplets, Atmos. Res. 63 (2006) 881–900.

[39] D. Kincaid, W. Cheney, Numerical Analysis: Mathematics of Scientific Computing, Thomson Learning, 2002, 788pp.

[40] Y. Xue, L.P. Wang, W.W. Grabowski, Growth of cloud droplets by turbulent collision-coalescence, J. Atmos. Sci. (2007), manuscript in preparation. Available from: http://research.me.udel.edu/lwang/reprints/Xue_etal_JAS_Jan_15_07.pdf.